TU Delft Delft University of Technology

Department of Precision and Microsystems Engineering

Actuator and sensor system design of a haptic parallel robot

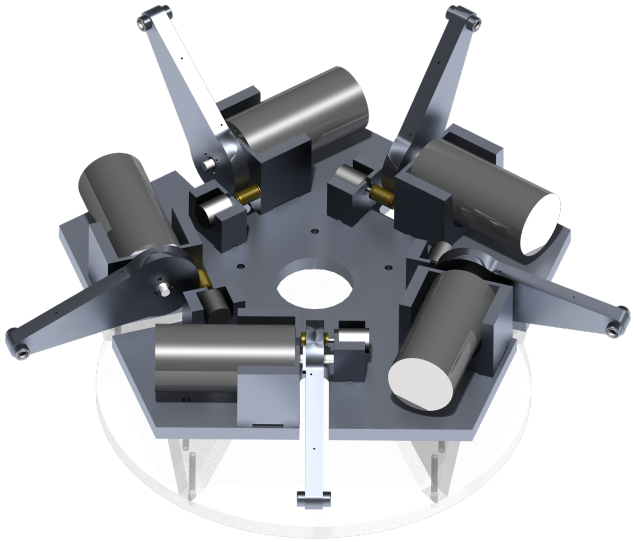

Name: O.S. van de Ven, BSc

Report no: ME 11.013
Coach: P. Lambert, MSc
Professor: prof. ir. R. H. Munnig Schmidt
Specialisation: Mechatronics
Type of report: Masters Thesis
Date: Delft, 3rd May 2011

Actuator and sensor system design of a haptic parallel robot

O.S. van de Ven, BSc

3rd May 2011

Preface

This thesis describes the main work that I have done on my final MSc. project at Delft University of Technology. My project is a part of the design of a haptic tele-operated microassembly system within the group of Precision and Microsystems Engineering (PME) at the faculty Mechanical, Maritime and Materials Engineering (3ME).

My work has focused on the final design of the haptic master part, which consists of a parallel robot structure designed by Patrice Lambert. I have done this work in cooperation with Johan Vogel, starting with a literature survey on the sensing and actuation capabilities of the human hand to define the system specifications, and the development of a rigid body as well as a finite elements model of the mechanical structure. This is all described in [vdVV11]. After finishing this first part, the work of Johan focused on the mechanical optimization and design of the robot structure, while my work was the analysis and design of the actuation and sensor system. This will be described here.

I would like to thank my supervisors Patrice Lambert, Hans Langen and my professor Rob Munnig Schmidt for their support during my work on the project and Jan van Frankenhuyzen, Rob Luttjeboer and Jo Spronck for their advice and help. Finally my thanks goes to Johan Vogel for the good cooperation.

Oscar van de Ven

May 2011

Contents

Chapter 1

Introduction

Within the development of a haptic tele-operated microassembly system a novel parallel robot structure is invented, which will be called *PentaGriph*. This structure will be used to make a haptic master device, capturing the motion of two fingers of the hand of a human operator while giving force feedback. When combined with a force-sensing micro-gripper slave robot, the user can perform a pick-and-place task, while feeling the interaction with the part and the environment. In the application of microassembly this master allows a user to perform low volume assembly tasks. Due to the force feedback the user can complete this task more accurately than what is currently possible.

The main advantage of using a parallel structure is that it allows heavy components such as actuators to be placed on the base instead of moving along with the mechanism, to reduce the effective robot inertia. In order to perform the assembly task, the haptic master interface is supposed to work with a user making a grasping motion. Therefore the robot structure allows a motion of the hand in 3 linear degrees of freedom (DOF): x, y and z, combined with a grasping and rotational motion of the fingers, defined by the grasping angle θ and half the fingertip distance ρ.

The structure of the robot, i.e. the configuration of links and joints is designed by Patrice Lambert and will be considered given. It consists of 5 parallel limbs called *lower limbs,* connected with a rotational joint to a rigid base and, on the other side to a parallelogram structure. This structure is connected to a platform consisting of 8 links and on top of them are two fingertips with which the user interacts with the robot. Figure 1.1 gives a schematic overview of this structure and Figure 4.1 shows the first prototype of this mechanism. More information on the mechanism can be found in [Lam10] and [vdVV11].

The design of the actuation and sensor system described in this thesis, starts in this chapter with the definition of the relevant specifications for the entire haptic master. The next important link is the analysis that converts these system specifications to the specifications of the actuator-sensor system. The method that has been created for that will be briefly presented in Chapter 2. A more complete overview of the method is available in Appendix B. When the component specifications are known, a conceptual and detailed design of the systems needed for actuation and sensing will be presented in Chapter 3. Chapter 4 covers the experiments performed with an earlier prototype of the PentaGriph mechanism. The final remarks and conclusions will be given in Chapter 5.

1.1 Problem statement

To use the given mechanism as a haptic interface, it has to be supplied with an actuation and measurement system. This report gives a description of the design of the sensor and actuator system that will be built into the next prototype. The following assignment defines the requirements of this actuator and sensor system:

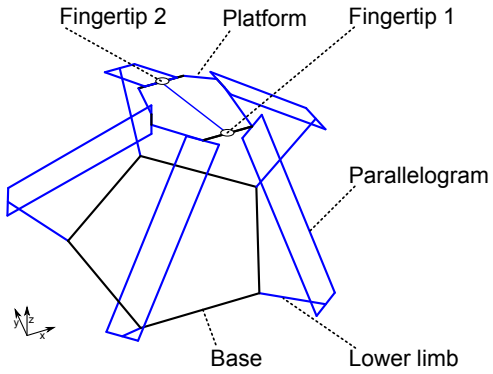

Figure 1.1: The PentaGriph structure and the part naming convention.

> Design an actuation and sensor system that gives sufficient and accurate kinesthetic force feedback to a user performing a grasping task with a haptic interface using the PentaGriph parallel mechanism.

The starting conditions of this design are defined by two important factors that are part of the problem statement. First the mechanism configuration is defined. The geometry of this specific structure is optimized such that the workspace of the robot is as large as possible while, remaining sufficiently far from singularities of the mechanism [Lam10]. This optimization fully defines the kinematics of the structure will therefore also be considered as known.[1]

Next 'sufficient kinesthetic force feedback to a user performing a grasping task' is mentioned. This implicitly defines the requirements on the actuation and sensing system. The user must be given sufficient and accurate force feedback for the task while he is not hindered geometrically or with parasitic forces. Also the absolute user position and motion must be measured with sufficient precision and accuracy. The literature survey in [vdVV11] investigated the meaning of this in terms of human sensing an actuation properties. In the next section the system specifications stated there will be converted into the actuation and sensing specifications.

1.2 System specifications

The system specifications mentioned in [vdVV11] have been adopted for the actuator and sensor system design. However a number of important changes and additions will be made.

The literature survey is not conclusive about appropriate values for user speeds and accelerations during pick-and-place tasks. Therefore a series of experiments is conducted using a Novint Falcon haptic interface device. Raw x, y and z position information has been captured while the test-persons made a typical pick-and-place motion with their hand. The goal was to determine typical hand velocities and accelerations that would occur during a grasping task. The results of this test, using 3 persons are given in Table 1.1b. More information about the data processing used to obtain these numbers from the position data can be found in [Vog11].

During the analysis of the required actuator forces needed to deliver the fingertip forces specified in [vdVV11], it appeared that the actuator size needed for that will strongly limit the performance in terms of parasitic forces. Also the experiment mentioned before showed that the velocity assumed in [vdVV11] used to define peak force was too high. Therefore the new peak fingertip force is now defined as the maximum comfortable working force of 7 N per finger. Gravity compensation of the human hand and arm is specifically not included

[1] The kinematics are defined by 11 geometric parameters. The values are listed in Appendix G.

Table 1.1: Summary of the global actuation and sensing specifications of the haptic interface.

(a) Specifications

Requirement	Quantity
Maximum force to the user finger	7 N
Largest disturbance force	0.3 N
Force feedback bandwidth	30 Hz
Position resolution	0.1 mm
Position accuracy	1 mm
Loop frequency	1 kHz

(b) Conditions

Condition	Quantity
Typical user speed	0.19 $\mathrm{m/s}$
Typical user acceleration	1.5 $\mathrm{m/s^2}$
Motion range	Scalene ellipsoid with radii of 80, 82 and 120 mm in x, y and z directions. $\theta = -\frac{\pi}{4} \ldots \frac{\pi}{4}$ rad and $\rho = 20 \ldots 40$ mm.

because also this would also significantly increase the actuator size and thus the parasitic forces.[2]

Additionally the motion range is updated to the ellipsoidal space of the new optimized mechanism and the total control-loop frequency is defined at 1 kHz, which is a generally accepted value for haptic systems. A summary of the finally used specifications is given in Table 1.1a.

1.3 Design considerations

Given the system specifications at the fingertips mentioned before, the specifications for the actuation and sensing system need to be derived. This will be done in Chapter 2, but first some basic design aspects have to be considered. These considerations will be evaluated when finally defining the actuator and sensor specifications in Section 2.4.

Actuator location The main reason for using a parallel structure for the robot is that it allows the stator part of the actuators to remain stationary with respect to the fixed world, reducing the moving mass and therefore the forces needed to move the structure. To achieve this the actuator has to act between the fixed world and the elements of the structure that are linked to the fixed world. In the given structure these are the lower limbs, connected with one rotational joint to the fixed world. Therefore the actuator should give a resulting torque around the shaft of this joint to use the advantage of the parallel robot. This defines the location of the actuator.

Sensor location The quantity that must be measured is the position of the fingertips of the robot. Since the main idea behind this robot structure is minimization of the effective inertia for the user, the measurement method must not introduce disturbing forces of a magnitude that will hinder the user. The position measurement system will, just as the actuation system,

[2] A solution for gravity compensation could be static balancing. This has been applied to the PentaGriph mechanism in [TvD11].

have two parts. The effective inertia of the moving part and the forces between the moving and the stationary part will have to be minimized in order to achieve this. In Appendix A a number of options available for position measurement are considered. Direct measurement of the fingertip positions has the practical implications that the measurement system would hinder the user or the user would obstruct the measurement. To limit the effective inertia and the weight of the structure the sensor system will not be entirely placed on a moving part. Therefore the sensor will measure the angle between the base and the 5 lower limbs of the structure. Therefore the sensors are located at the same joints as the actuators.

Actuator and sensor differences The PentaGriph mechanism requires actuation and measurement on 5 individual limbs. To limit the complexity of the analysis of the actuation and sensing specifications, it will be assumed that one actuation and sensor system design should fit in all 5 locations. Note that the mechanism is symmetric around the y-plane and that therefore only 3 different actuator and sensor locations can be distinguished.

Geometrical issues The idealized geometry of the parallel mechanism is given and therefore, with the relative sensor and actuator locations known, some geometrical requirements for the actuation and sensing system can be defined. The target location of these system is known and given the motion range of the mechanism the maximum space occupied can be derived. This space is a circle part of 72° and a radius of approximately 150 mm. Also the system should remain portable. Therefore the weight added by the actuation and sensor system must be limited.

Financial considerations Financial aspects can have a large influence on the design choices that will be made. This design will however be primarily focused on quality force feedback. The budget for building the prototype is limited, but will not be a major obstacle as long as the costs for individual components remain below an order of magnitude of € 1000.

Chapter 2

Component specifications

Since the actual sensing and actuation does not take place at the fingertips, the influence of the properties of the actuation and sensing systems on the fingertips must be determined. This chapter will explain the methodology used to transfer these system properties and how this affects the specifications of an individual actuator or sensor. The method can be applied to the PentaGriph mechanism, but can also be useful for analyzing other parallel actuated and measured robots and dual end-effector mechanisms.

Because the transfer of forces and speeds changes in space, it is not possible to review these transfers easily with a single numerical value. Therefore a rectangular grid of end-effector points in all 5 degrees of freedom is defined. For the points on this grid that lie within the workspace defined in [Lam10] all analysis results will be evaluated. All these results together form a result-distribution, of which a single numerical value will be generated by defining a border to these distributions such that 95% of the cases considered will be within this value. In general this means that if the sensing and actuation system fulfill the derived specification, the total system will perform according to the specifications in 95% of the points in space. Using a statistical method like this is necessary due to the large spread in results that will arise. This is because of the nature of the mechanism and the workspace in which it will be used. Using the extreme cases instead of the border of this interval would in certain cases lead to component specifications more than an order of magnitude higher. This is for instance the case with the needed maximum actuator torque. Increasing this torque would however require a heavier actuator, which would also increasing the disturbance forces on the user due to motor friction and inertia. Choosing the distribution factor does thus determine the balance between the average system performance and the ability to achieve the performance in the entire workspace.

2.1 Budgeting

The majority of the specification analysis will focus on the propagation of force and position related properties through the mechanism to determine the properties of the actuator and sensor system. The position measurement resolution will be entirely defined by the sensor system since it will be assumed that different positions at equal load should be distinguished. The accuracy will be equally divided between the error due to structural deformation and position measurement: both 0.5 mm.

Disturbance forces will come from both the structure and the actuator-sensor system, and they will share the total fingertip disturbance force budget of 0.3 N in three areas: static forces and forces dependent on speed and acceleration. It will be assumed that combinations of these areas occur infrequently and therefore each area has a total budget of 0.3 N. From experience it is known that static (friction) forces are a major problem for the actuator-sensor system and will therefore have a budget of 0.2 N. Inertia forces will be relatively large for

the structure so the actuator-sensor system gets a budget of 0.1 N assigned. The budget for viscous forces is also 0.1 N for the actuator-sensor.

2.2 Basic equations

Now that the properties at the fingertips are known, they can be transferred to the actuator and sensor location. In [vdVV11] the kinematics and the Jacobian of the robot were introduced and used. The basic equations needed for the further analysis of the specifications are summarized below.

$$\dot{\boldsymbol{\chi}} = \mathbf{J}\dot{\boldsymbol{q}} \tag{2.1}$$
$$\dot{\boldsymbol{q}} = \mathbf{J}^{-1}\dot{\boldsymbol{\chi}} \tag{2.2}$$
$$\boldsymbol{F} = \mathbf{J}^{-T}\boldsymbol{\tau} \tag{2.3}$$
$$\boldsymbol{\tau} = \mathbf{J}^{T}\boldsymbol{F} \tag{2.4}$$
$$\boldsymbol{\chi}(\boldsymbol{q}) = \mathbf{T}_{\mathrm{fwd}}(\boldsymbol{q})\,\boldsymbol{q} \tag{2.5}$$
$$\boldsymbol{q}(\boldsymbol{\chi}) = \mathbf{T}_{\mathrm{inv}}(\boldsymbol{\chi})\,\boldsymbol{\chi} \tag{2.6}$$

Where $\mathbf{J}$ is the Jacobian matrix, $\boldsymbol{\tau}$ is a vector of actuator torques, $\boldsymbol{F}$ is a vector of end-effector forces, $\dot{\boldsymbol{q}}$ is a vector of actuator speeds, $\dot{\boldsymbol{\chi}}$ is a vector of end-effector speeds, $\mathbf{T}_{\mathrm{fwd}}(\boldsymbol{q})$ is the forward kinematics function and $\boldsymbol{q}(\boldsymbol{\chi}) = \mathbf{T}_{\mathrm{inv}}(\boldsymbol{\chi})\,\boldsymbol{\chi}$ is the inverse kinematics function. Note that the end-effector variables $\boldsymbol{F}$ and $\boldsymbol{q}$ contain linear as well as rotational quantities. Also only the inverse kinematics can be computed directly, the forward kinematics must be computed using the inverse kinematics. In [vdVV11] also a special Jacobian is defined to determine the relation between general end-effector and Cartesian fingertip coordinates: $\mathbf{J}_{\mathrm{tip}}$. This means that the mechanism can be evaluated in (combinations of) three spaces: actuator angles $\boldsymbol{q}$ and torques $\boldsymbol{\tau}$, end-effector coordinates $\boldsymbol{\chi}$ and forces $\boldsymbol{F}$ and fingertip coordinates $\boldsymbol{\chi}_{\mathrm{tip}}$ and forces $\boldsymbol{F}_{\mathrm{tip}}$.

2.3 Specification transfer

From the foregoing equations the transfer of different quantities through the mechanism will be defined. These transfers will be evaluated using generalized load-cases which are defined based on the specifications of the entire system. The nature of these load-cases defines in which way the system specifications translate to the actuation and sensing subsystem. The analyses that have been done will next be considered one by one. Detailed computations and the full results for this mechanism can be found in Appendix B.

Motion range The motion range of the actuator and sensor are entirely defined by the inverse kinematics (2.6). From evaluating this this equation on the workspace-grid follows a set of actuator angles of which the limits define the motion range. A probability range should not be used here because the entire workspace should be reachable. Also excluding extreme actuator angles might exclude points of the workspace that are not at the border. The motion range is relative to the horizontal plane -42° until 85° for the ellipsoidal workspace and -90° until 90° for all reachable positions.

Sensor resolution In order to determine the sensor resolution, the smallest motion-step that a human is able to detect must also be seen by the sensor system. To determine the entire space in which the fingertips are able to move without a change in the sensor readout, the entire space spanned by all combinations of positive and negative actuator angle deviations are transferred from the actuator angle space to the fingertip space using 2.1. Note that

this assumes small angular deviations. This method of mapping the corners of a space between coordinate systems can be found in [Mer06]. The largest deviation in fingertip space determines the scale-factor needed to define the smallest detectable sensor step. Using a maximum fingertip displacement of 0.1 mm the sensor resolution should be $6.4 \cdot 10^{-5}$ rad for the 95% interval.

Maximum actuator torque Based on the maximum force of 7 N a user should be able to exert to the device, 34 load-cases on the fingertips of the device are defined and the actuator torques are computed using (2.4). This results for the 95% interval in an actuator torque of 2.3 Nm.

Maximum allowed static disturbance force Since static disturbance forces may be present at all actuators and sensor at the same time, the worst case is determined by evaluating all combinations of positive and negative unit disturbance torques at the actuator side using (2.3). The factor needed to scale down the worst case resulting fingertip force to within the error budget of 0.2 N determines the allowed disturbance. For the 95% interval this is $4.8 \cdot 10^{-3}$ Nm.

Actuator dynamic friction Using both Equations (2.2) and (2.3) it can be derived that the force on the user due to viscous damping in the actuator equals $\boldsymbol{F}_{friction} = c_{actuator}\mathbf{J}^{-T}\mathbf{J}^{-1}\dot{\boldsymbol{\chi}}$ (see also Equation (B.1)). To determine the end-effector velocities that are applied, it is assumed that disturbing actuator forces due to grasping and end-effector rotation velocities ($\dot{\rho}$ and $\dot{\theta}$) are negligible compared to the actuator motion due to end-effector motion ($\dot{x}$, $\dot{y}$ and $\dot{z}$). Therefore the typical user speed of 0.19 $^{\mathrm{m}}/_{\mathrm{s}}$ is applied in equally distributed directions in Cartesian space using a unity friction coefficient. The scaling factor between the magnitude of the fingertip forces and the maximum allowed budget of 0.1 N then determines the allowed friction coefficient. This is $1.44 \cdot 10^{-3}$ $\frac{\mathrm{Nm}}{^{rad}/_{\mathrm{s}}}$ for the 95% interval.

Actuator inertia In a way comparable to the dynamic friction, an equation for the force due to inertia of the actuator can be derived. There is however an extra term due to the dependency of the Jacobian on χ: $\boldsymbol{F} = \mathbf{I}_{actuator}\left(\mathbf{J}^{-T}\mathbf{J}^{-1}\ddot{\boldsymbol{\chi}} + \mathbf{J}^{-T}\dot{\mathbf{J}}^{-1}\dot{\boldsymbol{\chi}}\right)$. By considering only acceleration and no speed Equation (B.4) can be derived: $\boldsymbol{F} = I_{actuator}\mathbf{J}^{-T}\mathbf{J}^{-1}\ddot{\boldsymbol{\chi}}$. This can be evaluated in exactly the same was as the dynamic friction, only using a maximum acceleration of 1.5 $^{\mathrm{m}}/_{\mathrm{s}^2}$. With a force budget of 0.1 N this results in the 95% interval in $1.87 \cdot 10^{-4}\,\mathrm{kgm}^2$.

Note that the final equations for dynamic friction and inertia are very similar. When the force budgets are equal the ratio of the required inertia and damping coefficient equals the ratio of the maximum speed and acceleration. See Appendix B.3.2 for more details.

2.4 Specification summary

Based on the previous transformations and the other requirements the actuator and sensor specifications can be defined. Most specifications are first defined on a subsystem level in table 2.1a. The specifications for both actuator and sensor system is given in Tables 2.1b and 2.1c.

Next to the functional specifications there are also structural specifications. The stiffness of the lower limb that is defined in the mass-stiffness optimization of the structure in [Vog11] is added, as well as a quantification of the design considerations of Section (1.3).

Table 2.1: Overview of the actuator and sensor specifications.

(a) Actuation and sensing system specifications.

Specification	Value
Motion range	$-90°$ to $90°$
Motion range with specified accuracy and torque	$-42°$ to $85°$
Maximum static disturbance force	$5 \cdot 10^{-3}$ Nm
Maximum effective inertia	$1.87 \cdot 10^{-4}\,\mathrm{kgm}^2$
Maximum dynamic friction coefficient	$1.44 \cdot 10^{-3}\ \frac{\mathrm{Nm}}{\mathrm{rad/s}}$
Maximum weight	5 kg
Maximum size	$72°$circle part with radius 150 mm and no mechanism interference
Stiffness at the lower limb	$3.6 \cdot 10^{5}\ \frac{\mathrm{N}}{\mathrm{m}}$

(b) Actuator-specific specifications.

Specification	Value
Peak torque	2.3 Nm
Smallest actuator torque	$5 \cdot 10^{-3}$ Nm

(c) Sensor-specific specifications.

Specification	Value
Resolution	$6.4 \cdot 10^{-5}$ rad ($1.0 \cdot 10^{5}$ steps per revolution)
Accuracy	$6.4 \cdot 10^{-4}$ rad

Chapter 3

Design

The final design of the actuation and sensor system is defined next. The actuator and encoder part will be designed in detail. The current state of the design will be presented here and in more detail in Appendix D.

3.1 Actuation concepts

Now that the specifications of the actuation system are known, a solution that fulfills this must be found. A number of concepts that have been evaluated will be shortly introduced. A more thorough description of these concepts can be found in Appendix C. The required function of the actuation system is to supply a well defined torque to the lower limb of the structure, such that the desired force is exerted to the user.

The properties of this actuation subsystem are defined by the specifications in Section 2.4. When observing commercially available haptic interfaces like in [Nov11, Dim11] the actuation system contains mostly a conventional DC-motors and a transmission system. In Appendix C.1 an actuator transmission analysis has been done using available data from a number of motor-suppliers. It can be concluded that to achieve minimal parasitic forces a small transmission ratio must be used. In the extreme case this would mean application of an infinitely large motor and an infinitely small transmission ratio. However due to size limitations on the motor this will not be possible. Also every type of transmission will introduce unwanted forces, especially when large forces have to be passed through. Therefore using a motor with a large torque output that does not require a transmission and fits within the specified dimension would be recommended. By using a brushless type of motor the allowed output torques can be higher and the parasitic forces lower than with a brushed type motor. See Appendix C.2.1 for more details on these types of drives.

Other options to actuate the lower limb are the torque motor, the dual stage actuator and the linear drive. The torque motor has a too high inertia and a too small range for the purpose. The dual stage actuator increases the system complexity significantly while the advantages are limited.

To further decrease parasitic forces to the user a force control system can be implemented. The actuator torque can be measured to create a local force control loop. This however requires thorough adaptions to the actuator. By measuring the force at the user fingertips combined with a brushless DC direct drive actuator system, the actuator complexity does not increase and unwanted forces originating in the structure can be compensated as well. Control will however be more complex. Due to the added complexity and the fact that it could be added at a later stage, force control will not be implemented in the current design. In Appendix C.2.3 however a more conceptual design can be found.

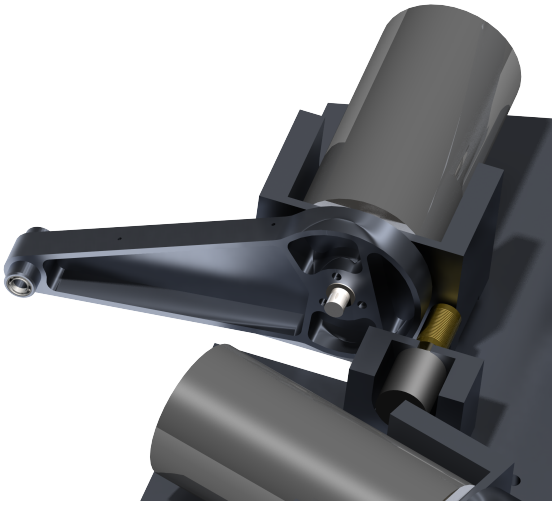

Figure 3.1: SolidWorks photorender of one of the actuator-sensor systems. The wire of the transmission and the plate that covers the lower limb are omitted.

3.2 Sensor concepts

In the design considerations of Section 1.3 it is decided that the sensor will measure the angle between the lower limb and the base-plate. The general options for this measurement are the direct measurement of the rotation and indirect measurement of a derived rotation or translation. Several options are linear and rotational encoders or potentiometers with and without a transmission and reflective systems. More details about these concepts are available in Appendix C.3.

In Appendix B.6 a more detailed analysis is performed to determine which points in space require extreme accuracies magnitudes. There is a significant relation between some of the coordinates in space, especially the grasping angle θ. For measurement however the relation between the required accuracy and the sensor angle $\boldsymbol{q}$ is relevant. It is shown that most of the points where a small resolution is needed occur at larger angles. In the distribution of all required sensor accuracies (not only the extremes) there are however no large angle dependencies visible. Therefore a system with an angle dependent sensitivity will not be used.

The final concept is the optical encoder, combined with a small transmission. This concept was chosen because of the small amount of unwanted forces that are introduced and the large motion range that is needed. The transmission is introduced to limit the needed encoder resolution so that the budget spent on encoders remains in balance with the cost of the rest of the prototype. The sensor transmission will be of the cable type. This will provide a play-free transmission that will prevent slip. A more extensive overview of the transmission options is available in Appendix C.1.

3.3 Sensor and actuator design

The detailed design of the sensor and actuator system entails the composition of the actuator, the encoder and the lower limb, with their connection to the base plate.

Transmission Using the direct drive motor concept and the rotary encoder with wire transmission, the detailed design of the actuation and sensing system can be made. Orientation on available rotary encoders that remain within the specifications, led to the conclusion that

the upper limit for the encoder resolution is around 5000 pulses per revolution. To minimize the required transmission, the quad-counts of the encoder will be used, resulting in an effective resolution of $\frac{2\pi}{5000 \cdot 4} = 3.1 \cdot 10^{-4}$ rad. Dividing by the required resolution gives an encoder transmission of $\frac{3.1 \cdot 10^{-4}}{6.4 \cdot 10^{-5}} = 4.9$. Using a small margin the transmission ratio is defined at 5.

The wire in the transmission is dimensioned at 0.5 mm so that the wire elongation under the largest load remains within the sensor resolution. The bus at the encoder around which the wire is wound has a spiraled groove with a radius larger than the wire to provide smooth winding of the wire, which appeared to be a problem with the fist prototype.

Lower limb The lower limb is the part that connects the structural design described in [Vog11] and the actuator-sensor design. Therefore there are also two sets of specifications that need to be fulfilled. From the structural side there are loads and maximum allowed displacements defining the effective stiffness and there is an inertia demand. From the actuator and sensor side a stiff connection has to be made to the actuator and, through the transmission, to the sensor.

Because of the structural demands the part is designed as a hollow structure and has a tapered shape. To obtain a stiff transmission a spoke structure has been made. Also the cable should have sufficient stiffness so that loads on the transmission, i.e. friction and inertia of the encoder, do not exceed the transmission position error budget. The wire runs over a large angle of more than $180°$, allowing the sensor to be placed low without limiting the motion range. This also results in a larger stiffness of the encoder suspension. The wire that is needed for the transmission runs over the circular part along a set of alignment pins. At one side the wire is attached using springs under a preload of the maximum expected force. To make the lower limb detachable from the motor a separate flange will be glued onto the motor shaft. This flange will be connected with 3 bolts to the lower limb. More details on the transmission design can be found in Appendix D.2.

Motor selection The actuation concept defined the use of a brushless DC motor. From a number of available motor manufacturers a motor type has been selected. For the specified maximum torque the stall torque can be used because this torque will only occur on a limited number of locations when the maximum force is requested. The Faulhaber 4490 048BS met the specifications in terms of torque at the time of the motor selection and is therefore chosen in the final design.[1] The main limiting point is the static friction torque, that is already comes close to the specification, while the encoder should still be included.

Encoder selection Because of the transmission that has been used, the encoder should have effectively 20000 positions on a single revolution. A quadrature encoder with 5000 cycles using all quad-counts like the selected Scancon 2MCA is therefore sufficient. The effective inertia of this encoder at the lower limb, including the effect of the transmission, is small compared to the rest of the system. Only the effective static friction torque is higher than the specified value, which appeared to be a problem with all feasible encoder types.

Because the encoder will be used in combination with a transmission, the index pulse of the encoder cannot be used, since it will occur more than once in the total stroke of the lower limb. To obtain the absolute position one reference point has to be defined within the stroke. From the available options a light barrier will be a good solution, because in an easy and relatively cheap way an accurate small range position measurement can be done to repeatably define the encoder zero. It also allows the reference measurement to take place within the motion range, because no objects need to obstruct the lower limb.

[1] Later corrections on the performed computations revealed that the actual actuator torques needed are slightly higher than predicted. Therefore the actuator will be able to exert the maximum torque roughly in 90% instead of 95% of all cases. These errors have been corrected in the computations results in this report.

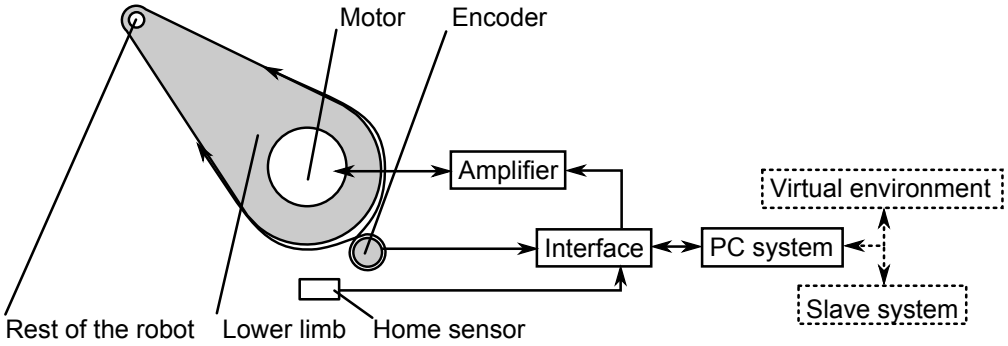

Figure 3.2: System overview of one of the five actuation and sensing systems. The dashed parts will not be considered as a part of the control system. Also the actual mechanism of the robot is omitted in this picture.

The light barrier that that defines the encoder zero must be able to position accurate up to $3.2 \cdot 10^{-4}$ rad to achieve 0.5 mm at the fingertips. Measuring half way the lower limb the position measurement accuracy is $16\,\mu\mathrm{m}$, which should be possible with a light barrier system. Physical positioning of this sensor may have a lower accuracy because the exact position can calibrated once.

Suspension If the motor is capable of suspending the lower limb within the specifications, a separate suspension system can be avoided, reducing the total disturbance forces due to friction on the system. Evaluating the motor data reveals that the allowed loads and the play are sufficient and therefore the motor suspension holds the motor and forms the main connection of the robot to the base plate. The inertia of the motor holder is not limited and therefore the effective stiffness should be an order of magnitude higher than the lower limb stiffness of $3.6 \cdot 10^5 \,\frac{\mathrm{N}}{\mathrm{m}}$. Also the motor suspension can be used to conduct heat from the motor to the base plate.

The most important requirement on the encoder holder is to maintain the position of the encoder in the direction of the cable. Since the inertia of this part is not limited, the same design as the motor holder has been used. The motor and the encoder are on opposite sides of the lower limb to limit the required size of the transmission disk, which in turn limits the inertia.

Base plate The base plate connects the actuators to the sensors as well as the lower limbs to each other. The stiffness of all these connections should be sufficient for these goals, but the inertia of this part is not limited. The 10 mm thick aluminum pentagon has slots to allow the required lower limb movement and a hole to guide the cables. Ribs on the bottom form the support of the platform and increase the stiffness.

3.4 Control system design

The other parts of the actuation and sensing system next to the actual sensors and actuator will be called the control system. It will contain the motor amplifiers, an interface card and a PC system, as well as the software that runs on the PC. The total system structure is depicted in Figure 3.2. The main control loop will be as follows: the encoder position is read out by the interface and sent to the PC system. The PC performs computations to obtain the absolute position and from that the end-effector position and the force transfer (the Jacobian matrix). A slave system of a virtual environment interprets the position information an responds with

a force command. This command is sent back to the PC system, is transformed using the Jacobian and through the interface and the amplifier to the motor. Commutation of the motor is performed by the amplifier. Therefore the amplifier receives position information from the hall sensors built into the motor.

3.4.1 Amplifier

The amplifier should be able to supply the motor stall current of 22.5 A in peak operation and the current control bandwidth must be more than the control bandwidth of 30 Hz. The dynamic range of the current control should be at least 10 bit and finally the amplifier must be able to perform the commutation of the motor. A suitable type would be the Maxon DES 70/10, which has a peak current of 30 A.

3.4.2 Interface and PC system

A flexible and easily programmable controller system is required to experiment with different controller structures. Therefore the system will run on standard PC hardware using a dedicated controller card. The real-time operating system xPC Target will run the controller and maintain the connection to the Matlab environment.

The interface should be able to externally receive information from 5 encoders, readout their light barrier calibration, send torque signals to 5 amplifiers and be compatible with the xPC Target system. The amplifiers will be of a digital type and can receive information through an analog port with an AD converter or via a digital CAN bus. To avoid using a series of converters (DA in the interface and AD in the amplifier) using a digital bus would be preferable. The bandwidth of the available bus is however not sufficient for transferring the 5 motor torques at the haptic refresh-rate of 1 kHz. Therefore an analog connection will be made. In Section B.2.3 the dynamic range is analyzed based on the minimum and maximum needed forces. In the 95% interval 10 bit DA conversion is needed.

For the encoders a readout and counter circuit will be needed to convert the encoder signals to usable information. The encoder homing has to be read out and since the light barrier will give a varying signal it needs an AD input per encoder. The homing of the different motors does not need to take place simultaneously, so these signal could be multiplexed into one input. Finally the total conversion time must be at least an order of magnitude below 1 ms to allow time for computations while running at 1 kHz.

Different considered solutions for the interface card are: separate analog, digital and encoder cards and all in one cards. Using multiple single purpose cards appeared to be a relatively expensive solution and would require a large PC system as well. The performance of the selected Quanser Q8 all-in-one card appeared to be sufficient and the costs lower than when using separate cards. More details can be found in Section D.11. The PC that will be running the system should have sufficient space for the interface card, an xPC Target supported network card and a recent processor. The TU Delft standard system: Dell Optiplex 780 is chosen.

3.4.3 Software structure

The software that runs the robot contains 5 main parts: the input, the kinematics, the force feedback, the compensation and the output part.

Input The input part reads the encoder and light barrier signals and computes the absolute angles of the lower limbs. Therefore it also includes the initial encoder zero definition using the light barrier.

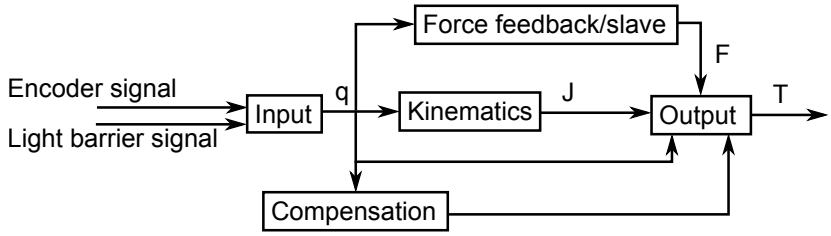

Figure 3.3: Schematic overview of the software structure. This is the content of the PC system block in Figure 3.2.

Kinematics The kinematics part performs the forward kinematics computation and uses the results to determine the Jacobian for further use in the controller part. The forward kinematics cannot be computed directly and therefore the iteration using the known inverse kinematics described in Appendix E.3 can be used. This iteration uses the properties of the Jacobian matrix to converge to the required position. For the real-time code it has to be decided if a 5-dimensional look-up table of precomputed values will be interpolated and used, or if the iteration can be performed real-time. Interpolation has the advantage of a constant computation time, however experiments have indicated that the iteration can probably be computed faster. Also at higher frequency the position difference between iteration steps is smaller, so that less iterations will be necessary. Therefore direct computation will be implemented.

The Jacobian will be computed in real time as well, because the computation is less intensive than the forward kinematics and interpolating is more complex due to the larger dimensions of the Jacobian.

Force feedback In the control part the computed positions and the Jacobian are used to determine the feedback force to the user. Finally this will contain the connection to the slave robot or the virtual environment, but there are also test structures present for implementing constant torques and forces and simulating different types of stiffnesses.

Compensation The compensation stage computes torques needed to overcome known but unwanted disturbance forces. To compute the required inertia and gravity torques, more information about the structure of the robot is needed. Therefore this work is part of [Vog11].

An important problem that arose in the component selection and is observed in the first prototype (Section 4.1) is static friction. The friction force can be experimentally defined as is done in Section 4.1.1, or based on component specifications. By applying a rapidly varying torque signal to a stationary actuator with an amplitude of the static friction, there is a moment within each period of the signal where friction torque is zero. This could help eliminating the effective friction.

Output The output stage merges all requested forces and torques together and computes the output voltage such that the correct torque will be exerted. Also the functional output of the controller stage will be limited such that the compensation structures will not suffer from saturation. To make sure that only the effective force magnitude and not the direction changes, all torque components should be decreased proportional when one of the torques saturates. Finally the output stage monitors the motor speeds and currents and turns them off when the speed or the estimated motor temperature becomes too high.

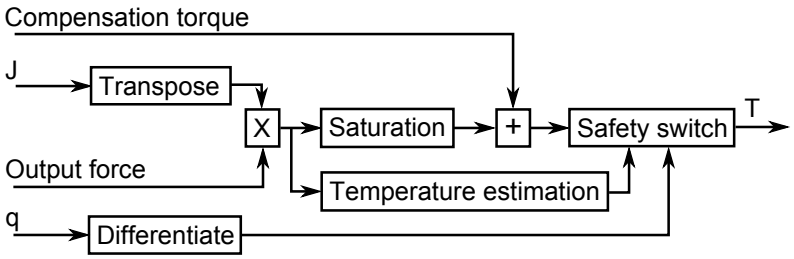

Figure 3.4: Schematic overview of the output stage. This is the content of the Output block in Figure 3.3.

Table 3.1: Planned mechanical system properties of the actuator-sensor system. Of all properties except the maximum force the extreme values excluding the 5% worst cases are given. For the maximum force the 10% worst cases are omitted. No force compensation is included.

Property	Value at		
	Lower limb	Fingertip (workspace extreme)	Fingertip (workspace average)
Inertia	$1.7 \cdot 10^{-5}\,\mathrm{kgm}^2$	$9.1 \cdot 10^{-3}\,\mathrm{N}$	$5.1 \cdot 10^{-3}\,\mathrm{N}$
Dynamic friction	$9.55 \cdot 10^{-6}\,{}^{\mathrm{Nm}}/_{\mathrm{rad}/\mathrm{s}}$	$6.6 \cdot 10^{-4}\,\mathrm{N}$	$3.7 \cdot 10^{-4}\,\mathrm{N}$
Static friction	$2.9 \cdot 10^{-2}$ Nm	1.2 N	0.90 N
Measurement resolution	$6.28 \cdot 10^{-5}\,\mathrm{rad}$	0.1 mm	$2.7 \cdot 10^{-2}\,\mathrm{mm}$
Maximum force	1.7 Nm	6.3 N	10 N

3.5 Final design performance

After evaluating the design choices, which is done in more detail in Appendix D.12, an overview of the performance of the planned system is made and given in Table 3.1. Note that the mentioned static friction is relatively high, but is must be noted that this is a worst case value based on the maximum expected encoder friction, which is the largest contribution to this value. However the static friction will still be one of the major problems of the current design that must be dealt with using friction compensation and/or a force control system.

Furthermore the accuracy is determined by the homing system and will be 0.5 mm at the fingertips in the 95% interval. Additionally the structure introduces on average 0.31 N at the fingertips and an average deformation of 0.35 mm. This can be derived from [Vog11]. The mass specification is also achieved with a mass of 0.94 kg per actuator-sensor system, or 4.7 kg in total.

Chapter 4

Practical work

For experimentation purposes a first prototype of the PentaGriph mechanism has been built, including actuators and encoders. The first prototype is used to implement and test the control system and perform the first experiments. For this an amplifier system and all other needed connecting components have been selected and installed. More details about the hardware of this prototype can be found in Appendix H. A second prototype was to be built using the optimized design described here and in [Vog11]. The majority of the parts of this prototype have also been manufactured, however the system is not yet entirely ready to be assembled.

4.1 First prototype

The first prototype has different geometrical parameters than the second prototype. An overview of these parameters is given in Appendix G. Another fundamental difference is that both the encoders and the motors act on the lower limb through a cable transmission of 14.8. For the encoders there is no reference measurement, but a physical stop is used to define the zero angle. For the Maxon 310007 DC motors a set of universal amplifiers has been selected: the Technosoft ISCM4805 DIN Intelligent Servo Module. These modules were programmed through their serial interface and CAN-busses to act as a controllable current source. The encoders and amplifiers were connected using custom made cables to the Quanser Q8 interface card.

With the prototype connected to PC the first steps could be made towards the implementation of the control system. This means implementing the control structure of Section 3.4.3 into a Matlab Simulink model. The model has the kinematics, control, output and compensation blocks of the control structure complemented with some XPC-Target monitoring and safety measures. The controller block contains a number of test structures, among others: fingertip position control, lower limb angle control and a virtual horizontal plane. With this setup a number of initial experiments have been performed. More information about the implementation of this control system is available in Appendix E.

While running the control system with the robot connected the kinematics computation algorithm needed typically 2 to 3 iterations to compute the end-effector position up to a lower limb angle error of $2 \cdot 10^{-4}\,\mathrm{rad}$, the sensor resolution[1]. Running the system at 1 kHz was no problem as long as the mechanism remained in the correct singularity.

[1] The prototype has a 500 pulse encoder and a transmission coefficient of 14.8.

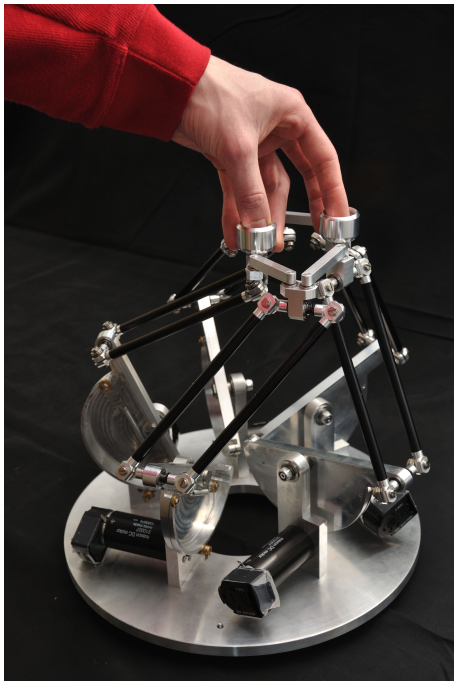

Figure 4.1: Picture of the first prototype without the control system attached.

Table 4.1: Friction measurement on the first prototype. The lower limb length is 85 mm. The friction torque is computed as half the difference between the minimum and the maximum torque. Half the difference between the average torques is a measure for the gravity torque, in this case: 0.065 Nm. Ideally a torque command of 0.40 Nm should result in a current of $\frac{0.40\,\mathrm{Nm}}{14.8125 \cdot 25.9 \cdot 10^{-3}\,\frac{\mathrm{Nm}}{\mathrm{A}}} = 1.043\,\mathrm{A}$. The average torque measured is 0.413 Nm.

Torque command [Nm]	Current [A]	Force [g] (Max./min.)	Avg. [Nm]	Friction [Nm]
-0.40	-1.040	625 / 515 ± 5	$0.475 \pm 4 \cdot 10^{-3}$	$0.046 \pm 4 \cdot 10^{-3}$
0.40	1.055	470 / 370 ± 5	$0.350 \pm 4 \cdot 10^{-3}$	$0.042 \pm 4 \cdot 10^{-3}$

4.1.1 Static friction experiment

In order to implement the static friction compensation a value for the friction has to be found. For this two types of experiments are set up. In both cases the parallelogram was not attached and the lower limb started in a horizontal position.

In the first experiment a torque set-point is set to one of the motors and with a spring-balance the force at the end of the lower limb is measured. By measuring the force needed to move up and down the static friction can be derived. Also by doing the measurement at a positive and a negative torque set-point, the effective gravitational torque is known. The results are given in Table 4.1. The average friction is $0.044 \pm 4 \cdot 10^{-3}$ Nm.

In a second test the motor is used to overcome static friction by applying a torque ramp and observing when the motor starts moving. Out of an average of 3 measurements the upwards torque is 0.051 Nm and the downwards torque -0.014 Nm. This means that the resulting friction torque is 0.033 Nm and the gravity torque is 0.019 Nm. Although the friction torques differ, it can be concluded that the static friction torque is of the order of magnitude of 0.04 Nm.

In these computations it is assumed that the friction torques upwards and downwards are equal, which is not verified. Also errors in the motor constant and the current control

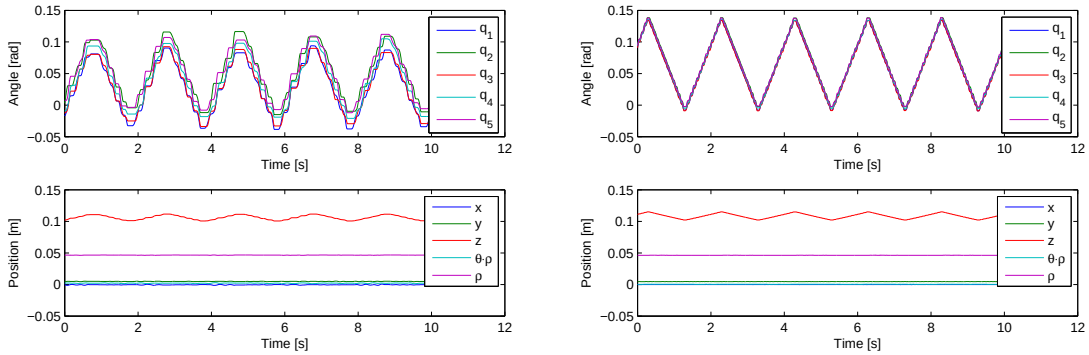

(a) Stiffness of 3 $\frac{\text{Nm}}{\text{rad}}$ and no damping.

(b) Stiffness of 7 $\frac{\text{Nm}}{\text{rad}}$ and added damping.

Figure 4.2: Visualization of stick-slip behaviour.

have influence on the last measurement. The first experiment showed however that these errors are not larger than 3% and 1% respectively. The friction torques derived in the different experiments are somewhat different, but the order of magnitude corresponds. The expected gravitational torque is however significantly different than the measured values. Based on the drawings of this prototype, the gravitational torque should be 0.009 Nm[2], while 0.065 Nm and 0.019 Nm is measured. Apparently another unidentified disturbance force plays a role. A possibility is a strong asymmetric static friction, for instance due to bearing damage.

4.1.2 Stick slip experiment

Due to the static friction in the prototype, stick-slip behaviour will occur. This becomes visible when a sawtooth set-point is set on the actuator angle controller as can be seen in Figure 4.2. As can be expected the magnitude of the error due to stick-slip can be decreased by increasing the controller stiffness and adding damping, see Figure 4.2b. For the haptic application this is however not an option. Therefore the application of the static friction compensation might help to reduce the stick slip behaviour, as can be seen in Figure 4.3. When no anti stick-slip signal is present the stick-slip behaviour is clearly visible. By adding a 0.04 Nm amplitude, which is the measured magnitude of the static friction, sinusoidal torque signal of 40 Hz, the stick-slip steps are clearly reduced. Increasing the magnitude of the signal even more to 0.08 Nm or 0.12 Nm seems to make the reduction somewhat larger, but also introduces unwanted vibrations. This can be seen to some extent in the graphs, but can be seen and felt very well. Note that the anti stick-slip signal is only added when the encoder position is constant. Therefore also the measurement resolution and accuracy influence the effectiveness of this compensation.

4.1.3 Observations

While performing the foregoing experiments and testing the internal controllers a number of problems of the first prototype occurred. First there are some problems with the wire transmission. The transmission disk built into the lower limb has a limited angle of somewhat less than $180°$. Therefore when a limb reaches $90°$ (straight upwards), the transmission suddenly stops and a large force is exerted to the wire, sometimes disassembling it. To prevent this in the second prototype an arc larger than $180°$has been used. Another combination of problems occurs because the transmission is used for actuation and because the wire is locked

[2]The lower limb has a mass of 57 g and a center of mass at 12 mm from the shaft. An additional rod of 3.14 g is placed at 85 mm

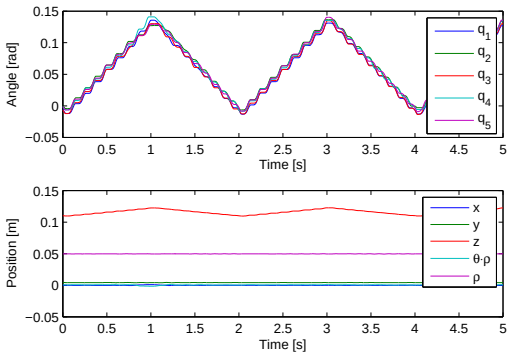

(a) Stiffness of 7 $\frac{\mathrm{Nm}}{\mathrm{rad}}$ and no anti stick-slip signal.

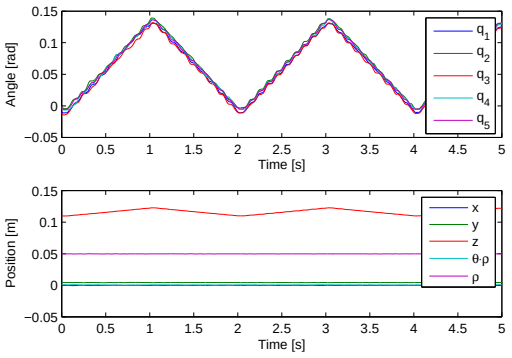

(b) Stiffness of 7 $\frac{\mathrm{Nm}}{\mathrm{rad}}$ and 0.04 Nm anti stick-slip signal.

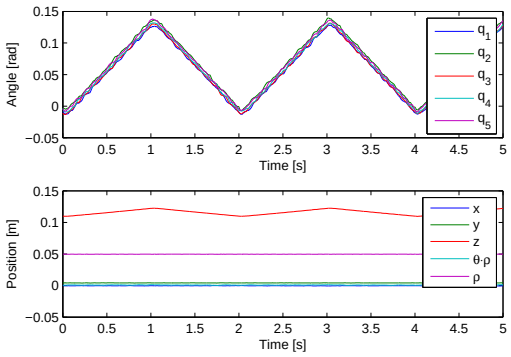

(c) Stiffness of 7 $\frac{\mathrm{Nm}}{\mathrm{rad}}$ and 0.08 Nm anti stick-slip signal.

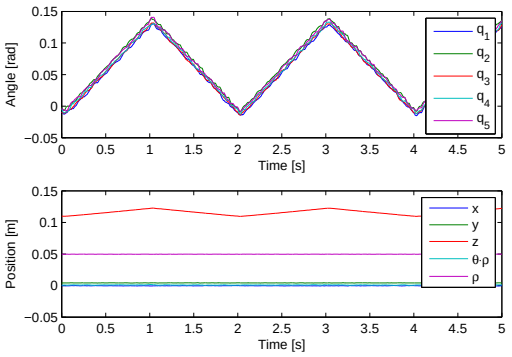

(d) Stiffness of 7 $\frac{\mathrm{Nm}}{\mathrm{rad}}$ and 0.12 Nm anti stick-slip signal.

Figure 4.3: Visualization of the influence of the anti stick-slip signal. In all experiments no damping is added.

to the lower limb using friction only. This causes the wire to slip at high forces, so that the position cannot be determined any more. This problem will not occur in the second prototype because the transmission is only used for measurement and the wire is connected to the lower limb using form closure.

With the motors of the prototype powered on, often a rattling sound can be heard. This sound appeared to come from the transmission and is probably due to the tight fit of the wire into the thread of wire bus. The wire is of a wound type and the dent in the wire bus has a radius equal to the wire, causing a scratching sound when the wire is pulled into the dent. This is solved by making the radius of the dent larger than the wire radius.

Finally strange behaviour is observer when the fingertips are rapidly moved upwards, towards the top of the workspace, with the amplifiers turned on and set to a zero current. The motors appear to push the lower limbs further into a different singularity. Note that at this point in space the actuators run relatively fast. Therefore the cause is probably that the amplifiers fail to counteract the motor EMF and keep the current zero. This is supported by the fact that the problem does not occur when the motors are disconnected. Note that the EMF is relatively high in this prototype due to the large transmission. Changing the current controller parameters of the amplifier might solve this problem.

4.2 Second prototype

The design of the new second prototype is described before and the parts have been drawn in SolidWorks. In Figure 4.4 a photo-render of the actuator and sensor system can be found. Most of the parts are also manufactured as can be seen on the pictures in Appendix D on the design details. The encoder homing system has not been entirely worked out in detail and drawn, but a homing system like the one used in the fist prototype can be used. This will however limit the position measurement accuracy.

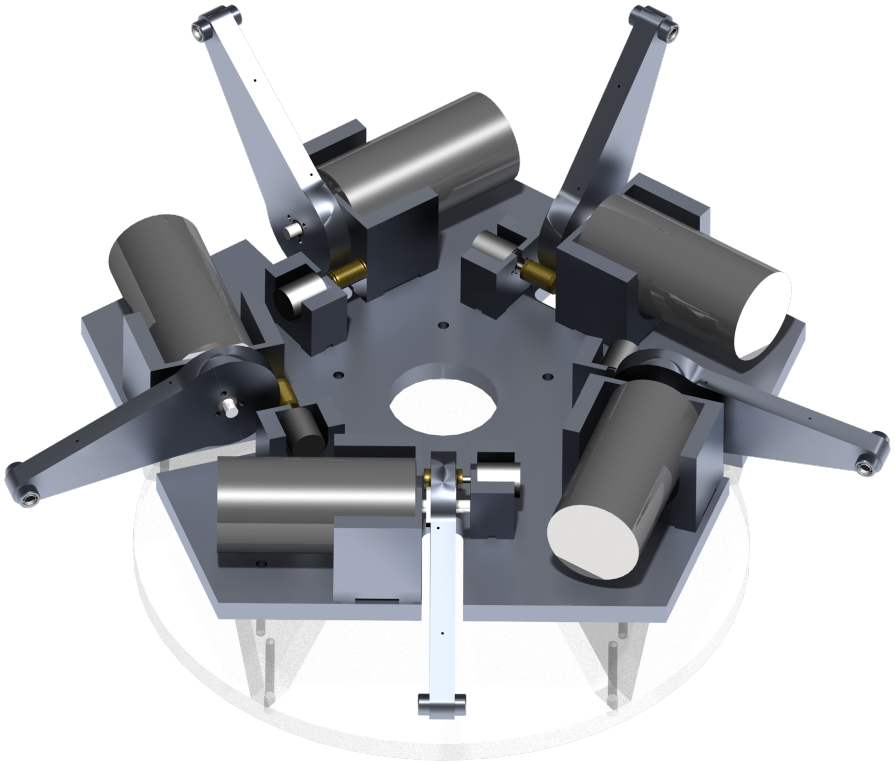

Figure 4.4: Photo-render of the actuator-sensor system.

Chapter 5

Discussion

5.1 Remarks and recommendations

Specifications propagation method Although the method of analysis of the specifications covers most important properties some additions and adaptations can be made to further improve the results. First of all the choice has been made to evaluate the system properties based on an interval that contains 95% of the evaluated points in space. Because the choice of this interval determines the balance between the performance and where it can be achieved, it would be interesting to investigate what the optimal balance is and how this optimum depends on the application of the robot.

In the current analysis force and motion propagation have been treated separately. There is however a mechanism that couples them: an error in the measured position also results in an error in the computed Jacobian. This subsequently leads to an error in the force reproduction. Some ideas to integrate this computation are given in Appendix B.5. With the current mechanism this effect can be assumed small, but when applying the method to other types of parallel robots, it should be included. If this computation is executed, the position derivative of the Jacobian is known. Then also the time derivative can be obtained so that the computation of the end-effector force due to actuator inertia in Appendix B.3.2 can be improved.

Another possible improvement of the specification analysis is using weighting to increase the relative importance of parts of the workspace that are more frequently used. For this the workspace usage should be analyzed in practice, for instance with the prototype, or a usage estimate can be made.

Design One of the most important issues with the current design is the presence of static friction. Next to implementing a compensation system as discussed, applying the force control loop discussed in Section C.2.3 will be a good next step in improving the friction behaviour. From a control perspective motor torque measurement will be the easiest to implement, but it requires a redesign of the actuation system. Fingertip force measurement can be implemented without thorough changes to the prototype but the control will be more difficult. Other options that make the design more interesting from a mechatronical point of view are the application of redundant force and/or position measurement. Combining multiple sets of sensors might result in lower specifications on each of them while the final performance increases.

At the start of the design process it is assumed that 5 identical sensor and actuator systems would be used to limit the complexity of the analysis. Now that the analysis is done it appears that there are differences in specifications for the individual actuators and sensors. Mainly the results of actuator and sensor 3 and, to a lesser extent 2 and 4, differ significantly. Therefore possibly an additional gain in performance can be obtained by allowing the dif-

ferent sensor and actuator systems to have different properties. For this particular robot the performance gain might be limited, but for other asymmetric parallel robots the gain might be significant.

Finally to improve the design the transmission could be modeled in more detail to obtain a more accurate estimate of the introduced disturbance forces and improve the design. Also these and other non-idealities could be incorporated into the available rigid body model of the system to determine the final implications on the system performance.

5.2 Conclusion

Starting from the specifications that a human operator imposes on a grasping haptic interface, an actuation and measurement system has been designed. To evaluate implications of the system specifications on the measurement and actuation subsystems an analysis method has been developed with which the propagation of the specifications through the mechanism can be determined. With this method the most important actuation and sensing properties of the parallel mechanism have been evaluated by using the Jacobian matrix evaluated in a number of points of the workspace and by application of well chosen force and displacement load-cases. Next to application to this specific mechanism, the method can also be applied to parallel actuated and measured robots in general.

Based on the subsystem specifications a design of the actuation and sensing is made that will be built into the second prototype of the PentaGriph mechanism. In order to minimize the disturbances to the user, a direct drive brushless DC motor is used for actuation. Position measurement is done with an optical encoder using a transmission ratio of 5 to achieve the required resolution. In this design the specification in terms of inertia and dynamic friction have been achieved, however the static friction remains a problem and should be solved by one of the suggested compensation methods. The basic control structure of this prototype has been designed and is implemented on the first prototype. With this setup some first measurements have been done to characterize the static friction behaviour in this prototype. Experiments in which a sinusoidal torque signal with the magnitude of the static friction has been added to compensate this, give promising results.

Appendix A

Comparison of sensor locations

The following list sums up a number of sensor principles and locations and their respective properties.

Measurement between the end-effector and the fixed world This is direct measurement of the needed quantity, which would be beneficial since the transfer of the mechanism would not influence the measurement. For this some sort of connection has to be made between the tips and the fixed world. This could be either physical, for instance with other links or wires, or with contactless techniques such as light. In both cases the freedom of motion of the user will however be limited, because the user is either blocked by the measurement or the user would block the measurement itself.

Measurement between two or more parts of the structure If relative distances or angles of elements of the structure are measured, a transfer could be chosen such that motions of the fingertips results in large changes in the sensor readings. It does however mean that the entire sensors will be placed on the structure, significantly increasing the effective inertia.

Measurement between a part of the structure and the fixed world This option suggests measurement between the lower limb and the fixed world, since they have only one free degree of freedom relative to each other. With this type of measurement the added inertia to the mechanism is limited and the user is not hindered more that necessary, however the entire motion transfer of the mechanism is included in the measurement.

Redundant measurement With redundant measurement more than 5 parameters will be measured to define the 5 DOF coordinates of the end-effector. This could for instance be measuring the lower limb angle and an angle on the parallelogram. This method could lead to interesting results, because two less accurate sensors might perform better than one more accurate sensor, but it also adds the disadvantages of both measurement locations. For instance the effective inertia will be relatively much increased. Finally processing the measurement data is more complex, because in each instance a choice needs to be made between more signals based on the accuracy of each signal.

Appendix B

Propagation of properties

The following appendix describes the methodology to transfer the end-effector properties of the parallel actuated and measured robot to the individual actuator and sensor properties. Note that in this method different coordinate systems have been used. More information about these coordinate systems and the way to transfer them to each other can be found in [vdVV11].

B.1 Motion range

The most important function needed when working with the range of the robot is the kinematics. Note that in most cases the inverse kinematics, to compute the actuator positions from the end-effector position, is known, while the forward kinematics isn't. To obtain information about the range, a rectangular space in all the dimensions of the end-effector space will be considered, in this case: $\chi \in \mathbb{R}^5$. On each point in the multidimensional grid the inverse kinematics are computed, resulting in the position of the actuated part of the mechanism.

The inverse kinematics is not necessarily valid in all points on the grid. The physical implication of the inverse kinematics being invalid is that the mechanism is unable to reach that given point in space. All point with a valid inverse kinematics together span a set which shows the total reachable space of the robot. A good indication that the entire reachable space is checked is that at the border of the entire set of valid points is enclosed by invalid points. It is however possible that a point that is not on the evaluated grid (it is placed between other points on the grid) gives the possibility to expand the reachable space, but if the grid is fine enough the image will be valid.

Since this specific robot will be operated by a human, the main interest is not in the first place all the points in space that can be reached, but a continuous logically shaped space in which the operator can safely move. For this purpose [Lam10] defined an ellipsoidal workspace based on singularity analysis. The space within this ellipsoid will be the basis of the analysis that will follow. Points outside the ellipsoid will not be part of the design-workspace and will thus not be considered further.

The distribution of the actuator angles is depicted in Figure B.2 for the entire reachable space and for the ellipsoidal workspace. From the graphs can be concluded that to be able to use the full range of the robot an actuator range of 180° is needed for all actuators. In the ellipsoidal workspace the actuator must be able to move from -42 ° to 86° or in other words with a total range of 128 °. Note that there are some differences between the individual actuators, but that due to symmetry the actuators 1 and 5 and 2 and 4 show the same behavior. This can also be observed in coming results. Figure B.1 shows the numbering convention used.

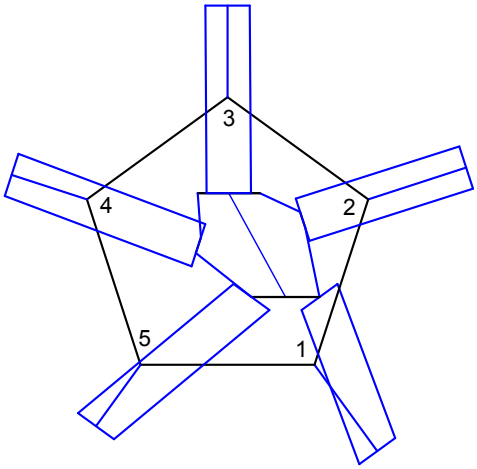

Figure B.1: Numbering of the PentaGriph lower limbs, actuators and encoders in a top view of the mechanism.

B.2 Actuator force

B.2.1 Maximum actuator torque

Load-cases In section 1.2 the maximum force on the end-effector is defined as 7 N. This is however the force magnitude that a human is supposed to be able to exert comfortably per finger and thus not a force load-case that can be directly inserted in the general Jacobian equations. In order to analyze the actuator torques needed, a number of load-cases must be defined. The goal of these load-cases is to analyze as good as reasonably possible, that is with a balance between computational work and validity of the results, what would be the torques needed to exert the maximum force to both fingertips in an arbitrary direction. The load-case used to test this contains the maximum force in a primary direction on both fingertips. Dependent on the stance of the platform a combination two tip-forces might give different results than the same combination on different tips (the forces of both tips interchanged). Therefore it is important to consider both the positive and the negative primary directions. This means that for each tip there are 6 possible force directions and all combinations consist of in total 36 load-cases. Note however that two of these load-cases consist of equal but opposite forces in z-direction. Since these directions are mechanically constrained these load-cases do not result in a load on the actuators and may therefore be excluded. This now results in 34 load-cases.

Another possibility to define load-cases must be used if next to a maximum force per finger, also a maximum force per hand should be considered. In this case the same combination of force directions is used but there is an added limitation on the magnitude. The vector sum of both fingertip forces should not exceed the maximum force per hand. In this case the limitation is not needed because the maximum hand-force is not limited to less than 14 N, but to apply it the following constraints should be used:

- If the two tip forces are in the same direction both should be the smallest of the maximum force per finger and half the maximum force per hand.
- If the two tip forces are in the opposite direction both should be the smallest of the maximum force per finger and the maximum force per hand.
- If the two tip forces are in orthogonal direction both should be the smallest of the maximum force per finger and $\frac{1}{\sqrt{2}}$ times the maximum force per hand.

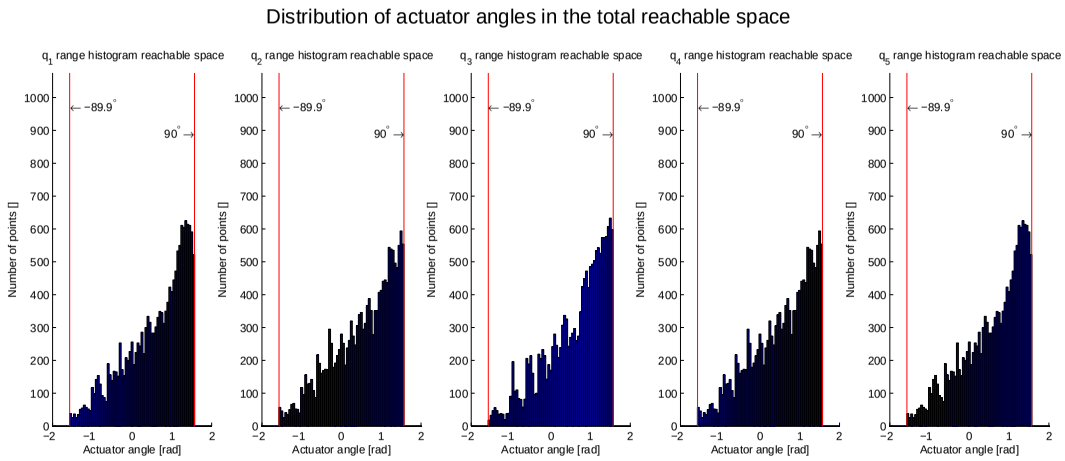

(a) Range of actuator angles when the total reachable space is considered down to a certain minimum height of the end-effector. The dataset analysed is a 5-dimensional rectangular space around the reachable space, limited by the plane $z = 0.1$ m, the gripper distances $4 \cdot 10^{-2}$ to $8 \cdot 10^{-2}$ and a maximum gripping angle of $\frac{\pi}{4}$. The grid has 9 points in each direction.

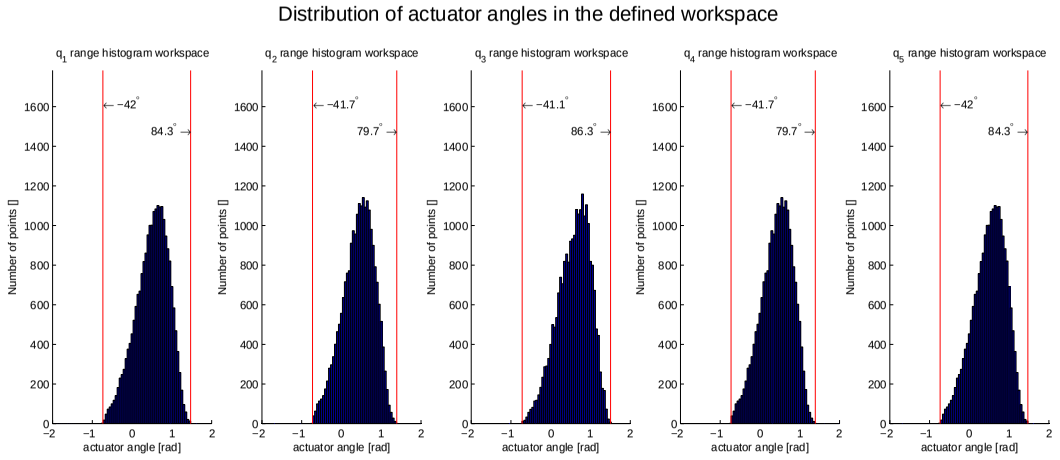

(b) Range of actuator angles when only the ellipsoidal space is considered. The dataset analysed is a 5-dimensional rectangular space around the half ellipsoid and a maximum gripping angle of $\frac{\pi}{4}$. The grid has 9 points in each direction.

Figure B.2: Range of actuator angles for all 5 actuators.

The load-cases are now defined in two Cartesian coordinate systems, one for the force of each finger. These forces need thus to be rewritten in terms of the general robot coordinates to use them in the force propagation equations. This coordinate transformation is a function of the 5-component end-effector position, or more precisely, dependent on the gripping angle and distance θ and ρ.

Force propagation Once the load-cases are defined the following force expression can be used.

$$\boldsymbol{\tau} = \boldsymbol{J}^T \boldsymbol{F}$$

This expression must be evaluated on all the necessary point in space and for all the load-cases, converted to the correct coordinate system. This will then result in the distribution of actuator torques needed to give maximum force feedback to the user. The results found are depicted in Figure B.3. Note that due to symmetry the results of actuator pairs 1 and 5 and 2 and 4 are again identical.

B.2.2 Maximum allowed static disturbance force

The maximum disturbance force is the largest unwanted force that will be allowed from the actuator and sensor system. This quantity will be based on the largest static friction force budget on the user that is specified as 0.2 N.

To determine this maximum disturbance torque it might seem logical to apply a method similarly to the one in Section B.2.1. However the following adaption should be made: instead of defining load-cases that the actuation system should be able to handle, maximum load-cases have to be defined. These load-cases should then consist of maximum forces to the user in certain chosen directions. The smallest torque computed in this way would then be a measure for the maximum allowed torque. It is however very well possible that for a certain chosen load-case in a certain position, the transfer form the actuator to the end-effector is such that zero force is required from a certain actuator. This method would then result in a maximum torque of zero, which is not valid. The problem originates from the the fact that the chosen direction does not have to be the limiting direction in terms of disturbance forces. To overcome this problem the analysis will be done the other way around: from the side of the actuator instead of the user.

To determine the limiting torque now a number of load-cases will be applied to the actuators directly and the resulting forces to the fingertips will be evaluated. Assuming that all actuator/sensor systems will be equal, unit torques will be applied. The load-cases are different combinations of these unit forces, the largest resulting fingertip force determines the scaling needed to remain within the limit that has been set. The dataset consists of all possible combinations of positive and negative unit torques. Load-cases with zero torques do not need to be considered since the force transfer computations are linear and thus the result will always be between the plus and minus unity load-case. In total there are $2^5 = 32$ combinations of plus and minus one. [1]Within this set there are however duplicates: half of the cases are equal to the other half, only negative. Since the force transfer is entirely linear for a given end-effector position, these duplicate load-cases can be eliminated without influencing the result. The load-cases are defined as the columns of τ_{LC}:

[1]Note that this method is similar to the method that can be found in [Mer06] to transfer the boundaries of a multidimensional volume from one space to another. Only now the method is used with a 'volume' in force coordinates.

Figure B.3: Actuator torques needed for maximum feedback force. The columns represent the torques of the 5 actuators and the last column is represents the maximum torque of the 5 actuators for each point on the grid. The top row shows the frequency with which an actuator load occurs in a histogram. The second row uses the same data, but in a cumulative histogram. Also the torque below which 95% and 99% of all points and load-cases can be found are indicated. The bottom row shows on the x-y plane the locations of the torques higher than the indicated 95% level. The magnitude of a torque is proportional to the size of the circle and changes from blue to red for higher torques.

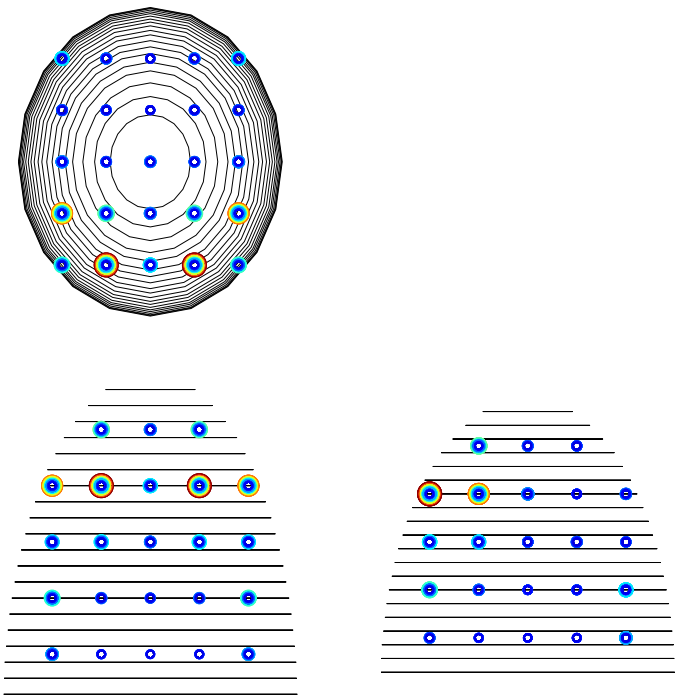

Figure B.4: Locations of the 5% highest torques in 3 dimensions. Each point in space represents all θ and ρ values.

$$\tau_{\mathrm{LC}} = \begin{bmatrix} -1 & -1 & -1 & -1 & -1 & -1 & -1 & -1 & -1 & -1 & -1 & -1 & -1 & -1 & -1 & -1 \\ -1 & -1 & -1 & -1 & -1 & -1 & -1 & -1 & 1 & 1 & 1 & 1 & 1 & 1 & 1 & 1 \\ -1 & -1 & -1 & -1 & 1 & 1 & 1 & 1 & -1 & -1 & -1 & -1 & 1 & 1 & 1 & 1 \\ -1 & -1 & 1 & 1 & -1 & -1 & 1 & 1 & -1 & -1 & 1 & 1 & -1 & -1 & 1 & 1 \\ -1 & 1 & -1 & 1 & -1 & 1 & -1 & 1 & -1 & 1 & -1 & 1 & -1 & 1 & -1 & 1 \end{bmatrix}$$

These load-cases are evaluated on a grid of end-effector positions using the expression

$$\boldsymbol{F} = \boldsymbol{J}^{-T}\boldsymbol{\tau}$$

Then the end-effector force is split into two tip forces with 3 orthogonal coordinates each. Note that this results into 6 force components while only 5 independent components are known. This is because the two fingertips are kinematically constrained by the platform in z-direction. In order to obtain valid results the force in z-direction is equally distributed over both tip, implicitly adding one equation so that the 6th variable in the system can also be solved for.

If the tip forces $\boldsymbol{F}_{\mathrm{tip},1}$ and $\boldsymbol{F}_{\mathrm{tip},2}$ are known the allowed actuator torque can be determined as follows for both tips:

$$\tau_{\mathrm{dist,max,tip\#}} = \frac{F_{\max}}{|\boldsymbol{F}_{\mathrm{tip\#}}|}$$

The largest tip force is limiting and therefore the final maximum disturbance torque is in each point computed as:

$$\tau_{\mathrm{dist,max}} = \frac{F_{\max}}{\max\left(|\boldsymbol{F}_{\mathrm{tip1}}|, |\boldsymbol{F}_{\mathrm{tip2}}|\right)}$$

These values are given in a histogram in Figure B.5a. When 95% of all points in the workspace should have a disturbance force of less than 0.2 N, the disturbance torque must not exceed $5 \cdot 10^{-3}$ Nm. Figure B.5b then gives the distribution of the fingertip forces assuming this value.

B.2.3 Dynamic range

The ratio of the largest and the smallest needed actuator torque determines the range and the resolution of the amplifier. Figure B.6 gives an overview of this dynamic range. The smallest needed torque is defined as the same torque as the largest disturbance torque since it is on the border of what can be felt.

B.3 Inertia and friction

The actuator and sensing system itself also has inherent disturbing forces which will ultimately lead to disturbances to the user. The inertia of this system and the dynamic friction will be considered. These phenomena are discussed together because it will follow that the computations involved will be, under certain assumptions, quite similar.

B.3.1 Dynamic friction computation

Dynamic friction in the actuation and sensor system, described with the parameter c_{actuator}, results in a friction torque of $\tau_{\mathrm{friction}} = c_{\mathrm{actuator}}\dot{q}$. Generalizing this for all actuators gives:

$$\boldsymbol{\tau}_{\mathrm{friction}} = \mathbf{C}_{\mathrm{actuator}}\dot{\boldsymbol{q}}$$

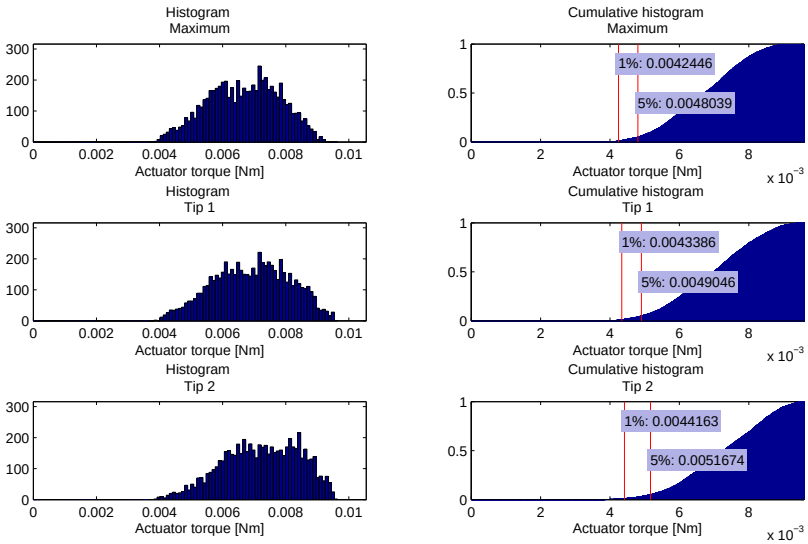

(a) Allowed static disturbance torque.

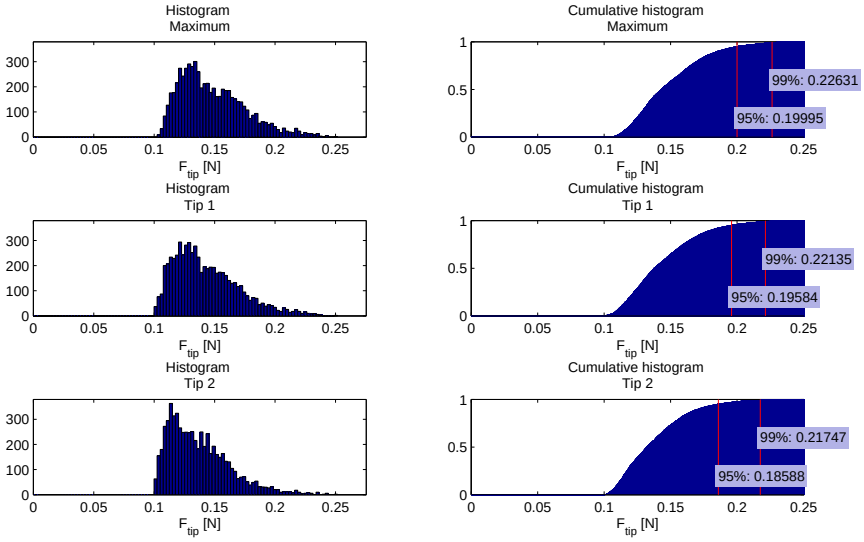

(b) Tip forces due to static disturbance forces.

Figure B.5: Maximum disturbance torque.

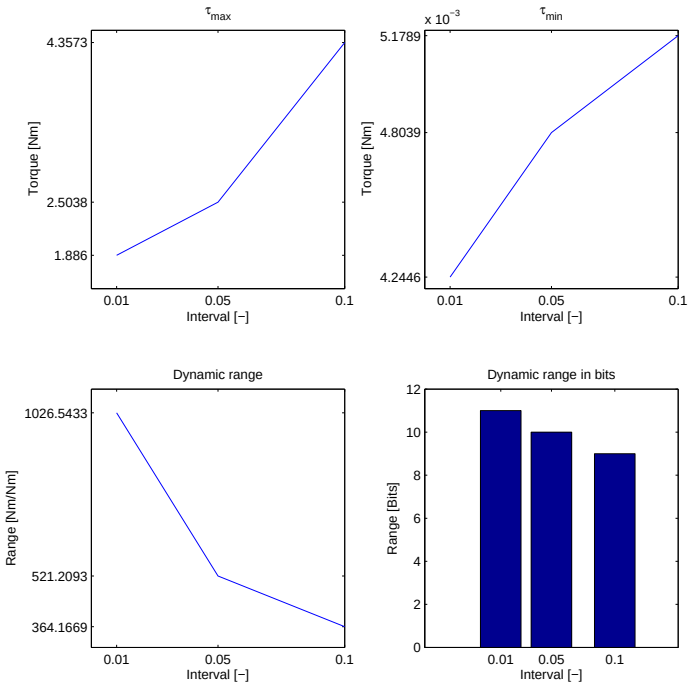

Figure B.6: Dynamic range of the actuator as a function of the chosen interval.

where $\mathbf{C}_{\text{actuator}}$ is a dynamic friction matrix, with on the diagonal the dynamic friction-coefficients. From Section 2.2 it is known that

$$\dot{\boldsymbol{q}} = \mathbf{J}^{-1}\dot{\boldsymbol{\chi}}$$

so that

$$\boldsymbol{\tau}_{\text{friction}} = \mathbf{C}_{\text{actuator}}\mathbf{J}^{-1}\dot{\boldsymbol{\chi}}$$

An actuator torque then translates to an end-effector force according to

$$\boldsymbol{\tau} = \mathbf{J}^{T}\boldsymbol{F}$$

so that

$$\begin{aligned}\mathbf{J}^{T}\boldsymbol{F}_{\text{friction}} &= \mathbf{C}_{\text{actuator}}\mathbf{J}^{-1}\dot{\boldsymbol{\chi}}\\ \boldsymbol{F}_{\text{friction}} &= \mathbf{J}^{-T}\mathbf{C}_{\text{actuator}}\mathbf{J}^{-1}\dot{\boldsymbol{\chi}}\end{aligned}$$

If all actuation systems are equal, this relation can be simplified to

$$\boldsymbol{F}_{\text{friction}} = c_{\text{actuator}}\mathbf{J}^{-T}\mathbf{J}^{-1}\dot{\boldsymbol{\chi}} \tag{B.1}$$

because then $\mathbf{C}_{\text{actuator}} = c_{\text{actuator}}\mathbf{I}$. In other words this means that the effective dynamic friction matrix in end-effector coordinates is:

$$\mathbf{C}_{\text{effective}} = c_{\text{actuator}}\left(\mathbf{J}\mathbf{J}^{T}\right)^{-1} \tag{B.2}$$

B.3.2 Inertia computation

Assuming that the actuation and sensing system has an effective angular inertia around the shaft of I_{actuator}, the disturbance torque at this shaft is:

$$\boldsymbol{\tau}_{\text{inertia}} = I_{\text{actuator}}\ddot{q}$$

with

$$\ddot{q} = \frac{d\dot{q}}{dt} = \frac{d^2q}{dt^2}$$

This can be expanded to the form for all actuators, using $\mathbf{I}_{\text{actuator}}$ as a diagonal matrix of actuator inertia's:

$$\boldsymbol{\tau}_{\text{inertia}} = \mathbf{I}_{\text{actuator}}\ddot{\boldsymbol{q}} \tag{B.3}$$

From Section 2.2 it is known that

$$\dot{\boldsymbol{q}} = \mathbf{J}^{-1}\dot{\boldsymbol{\chi}}$$

so that

$$\ddot{\boldsymbol{q}} = \mathbf{J}^{-1}\ddot{\boldsymbol{\chi}} + \dot{\mathbf{J}}^{-1}\dot{\boldsymbol{\chi}}$$

Filling this in in (B.3) gives

$$\boldsymbol{\tau} = \mathbf{I}_{\text{actuator}}\left(\mathbf{J}^{-1}\ddot{\boldsymbol{\chi}} + \dot{\mathbf{J}}^{-1}\dot{\boldsymbol{\chi}}\right)$$

Then the end-effector forces also follows from Section 2.2:

$$\begin{aligned}\boldsymbol{F} &= \mathbf{J}^{-T}\boldsymbol{\tau} \\ &= \mathbf{J}^{-T}\mathbf{I}_{\text{actuator}}\left(\mathbf{J}^{-1}\ddot{\boldsymbol{\chi}} + \dot{\mathbf{J}}^{-1}\dot{\boldsymbol{\chi}}\right) \\ &= \mathbf{I}_{\text{actuator}}\left(\mathbf{J}^{-T}\mathbf{J}^{-1}\ddot{\boldsymbol{\chi}} + \mathbf{J}^{-T}\dot{\mathbf{J}}^{-1}\dot{\boldsymbol{\chi}}\right)\end{aligned}$$

If we then neglect the end-effector speed $\dot{\boldsymbol{\chi}}$ (we consider the case of acceleration only), the inertia force may be simplified to:

$$\boldsymbol{F} = \mathbf{J}^{-T}\mathbf{I}_{\text{actuator}}\mathbf{J}^{-1}\ddot{\boldsymbol{\chi}}$$

This assumption has been made because at the present the time derivative of the Jacobian matrix was unknown. An estimate of the error made by using this assumption can be made based on [Vog11], where for a more limited set of load-cases (only primary Cartesian directions of motion) average forces due to inertia in case of an end-effector speed and acceleration are both evaluated. Using the same speeds and accelerations, the force due to speeds are about 27% of the total force due to inertia. [2] Another simplification can be made by assuming that the inertia of all actuators is equal. Then:

$$\boldsymbol{F} = I_{\text{actuator}}\mathbf{J}^{-T}\mathbf{J}^{-1}\ddot{\boldsymbol{\chi}} \tag{B.4}$$

or the effective inertia matrix in end-effector coordinates is:

$$\mathbf{I}_{\text{effective}} = I_{\text{actuator}}\left(\mathbf{J}\mathbf{J}^{T}\right)^{-1} \tag{B.5}$$

Note that this is the 'same' relation as for dynamic friction in Equation (B.2). Therefore the effective inertia can be derived from the effective dynamic friction and vice versa. Compare for instance Equations (B.2) and (B.5). If the friction and inertia force in Equations (B.4) and (B.1) are compared it can be concluded that:

$$\begin{aligned}\frac{\boldsymbol{F}_{inertia}}{\boldsymbol{F}_{dynamic\,friction}} &= \frac{I_{actuator}\mathbf{J}^{-T}\mathbf{J}^{-1}\ddot{\boldsymbol{\chi}}}{c_{actuator}\mathbf{J}^{-T}\mathbf{J}^{-1}\dot{\boldsymbol{\chi}}} \\ &= \frac{I_{actuator}\ddot{\boldsymbol{\chi}}}{c_{actuator}\dot{\boldsymbol{\chi}}}\end{aligned}$$

Therefore only dynamic friction *or* inertia has to be evaluated if the speed and acceleration load-cases are of equal form.

[2] The forces are per unit of inertia are due to accelerations: 628 N/kgm^2 and due to speed: 229 N/kgm^2.

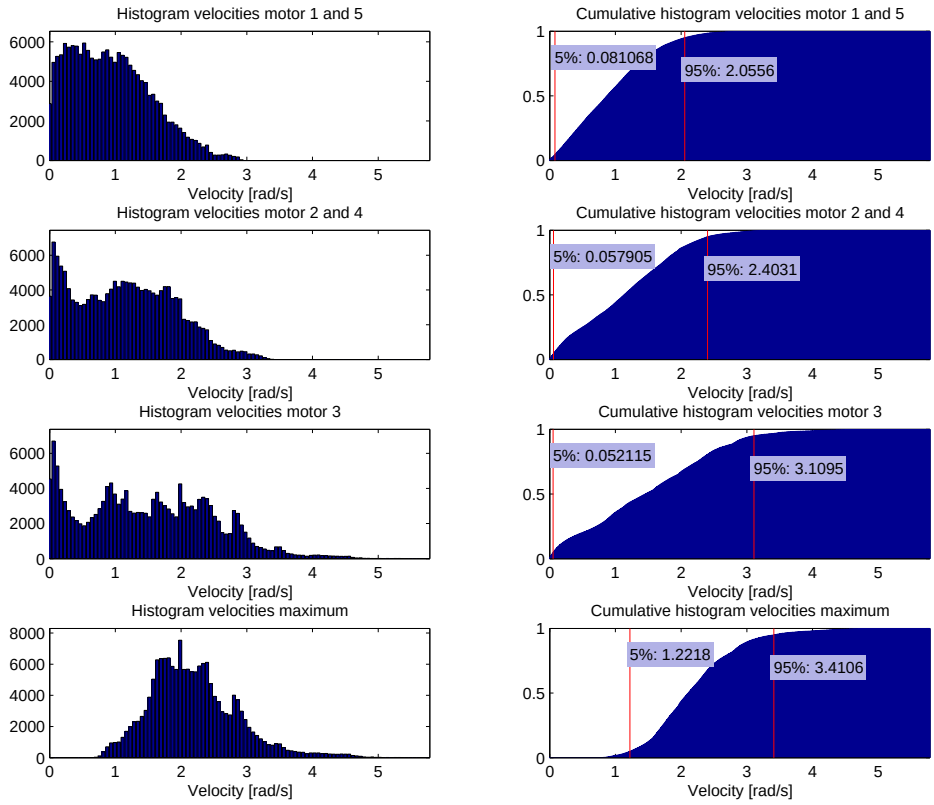

Figure B.7: Actuator velocity distribution.

B.3.3 Load-cases

To determine end-effector forces that will occur during motion and acceleration first an important assumption will be made: disturbing actuator forces due to grasping and end-effector rotation ($\dot{\rho}$ and $\dot{\theta}$) are negligible compared to the forces due to end-effector motion ($\dot{x}$, $\dot{y}$ and $\dot{z}$). This may be due to three reasons: (1) the speeds $\dot{\rho}$ and $\dot{\theta}$ themselves are relatively small, (2) the transfer from these motions to $\dot{\boldsymbol{q}}$ is small and (3) the force transfer from these actuator motions to end-effector forces are small. Since there is no specific data available on the grasping and rotation speed, the validity of this assumption must be verified with observations. When making a typical grasping motion using the first prototype (Section 4.1) it can indeed be observed that friction forces and actuator movements in these directions are relatively small. Therefore this assumption will be considered valid. Note that it follows from the foregoing that this is also valid for inertia forces since they use the same transfer.

The load-cases that will be evaluated for the actuator inertia and dynamic friction consist of end-effector motions and accelerations in x, y and z directions, but also combinations of 2 and 3 of these directions are evaluated. Together this are 26 velocity and acceleration load-cases: 6 for the primary directions, both positive and negative, 12 combinations of 2 of them and 6 combinations of all 3 directions. These cases are the columns of C_1, C_2 and C_3:

$$C_1 = \begin{bmatrix} 1 & 0 & 0 & -1 & 0 & 0 \\ 0 & 1 & 0 & 0 & -1 & 0 \\ 0 & 0 & 1 & 0 & 0 & -1 \end{bmatrix}$$

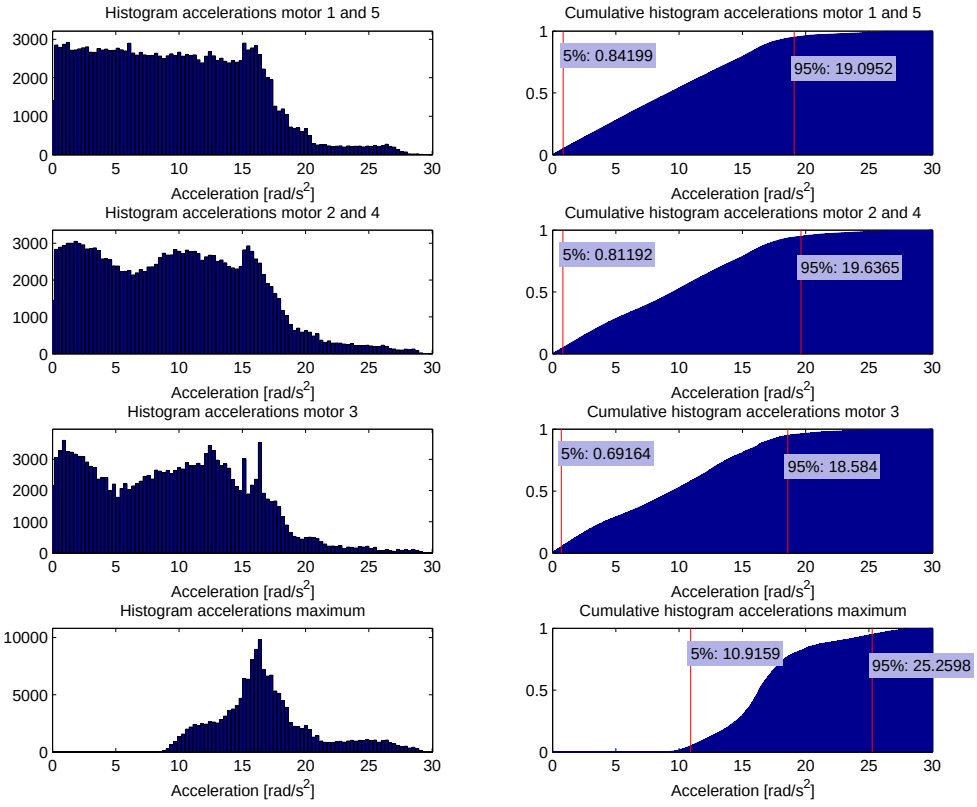

Figure B.8: Actuator acceleration distribution.

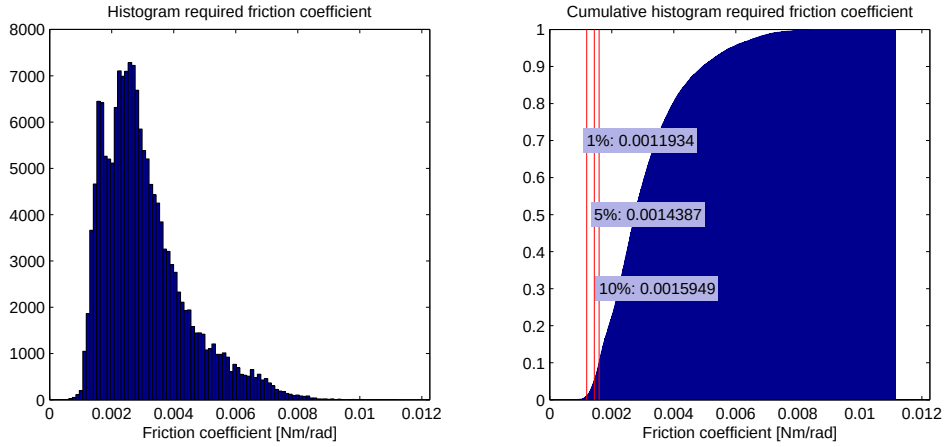

Figure B.9: Maximum allowed dynamic friction coefficient.

$$C_2 = \begin{bmatrix} \frac{\sqrt{2}}{2} & 0 & \frac{\sqrt{2}}{2} & -\frac{\sqrt{2}}{2} & 0 & \frac{\sqrt{2}}{2} & \frac{\sqrt{2}}{2} & 0 & -\frac{\sqrt{2}}{2} & -\frac{\sqrt{2}}{2} & 0 & -\frac{\sqrt{2}}{2} \\ \frac{\sqrt{2}}{2} & \frac{\sqrt{2}}{2} & 0 & \frac{\sqrt{2}}{2} & -\frac{\sqrt{2}}{2} & 0 & -\frac{\sqrt{2}}{2} & \frac{\sqrt{2}}{2} & 0 & -\frac{\sqrt{2}}{2} & -\frac{\sqrt{2}}{2} & 0 \\ 0 & \frac{\sqrt{2}}{2} & \frac{\sqrt{2}}{2} & 0 & \frac{\sqrt{2}}{2} & -\frac{\sqrt{2}}{2} & 0 & -\frac{\sqrt{2}}{2} & \frac{\sqrt{2}}{2} & 0 & -\frac{\sqrt{2}}{2} & -\frac{\sqrt{2}}{2} \end{bmatrix}$$

$$C_3 = \begin{bmatrix} \frac{\sqrt{3}}{3} & \frac{\sqrt{3}}{3} & \frac{\sqrt{3}}{3} & \frac{\sqrt{3}}{3} & -\frac{\sqrt{3}}{3} & -\frac{\sqrt{3}}{3} & -\frac{\sqrt{3}}{3} & -\frac{\sqrt{3}}{3} \\ \frac{\sqrt{3}}{3} & \frac{\sqrt{3}}{3} & -\frac{\sqrt{3}}{3} & -\frac{\sqrt{3}}{3} & \frac{\sqrt{3}}{3} & \frac{\sqrt{3}}{3} & -\frac{\sqrt{3}}{3} & -\frac{\sqrt{3}}{3} \\ \frac{\sqrt{3}}{3} & -\frac{\sqrt{3}}{3} & \frac{\sqrt{3}}{3} & -\frac{\sqrt{3}}{3} & \frac{\sqrt{3}}{3} & -\frac{\sqrt{3}}{3} & \frac{\sqrt{3}}{3} & -\frac{\sqrt{3}}{3} \end{bmatrix}$$

These cases have all a magnitude of 1 and will be multiplied with the expected velocities and accelerations that occurs during the grasping motion. These values are given in Table 1.1b and have been derived from a small experiment where 3 users made typical 3 DOF motions that would occur when doing a pick-and-place task. This results in a velocity and acceleration distribution of the actuators as given in Figures B.7 and B.8. The analysis results in terms of dynamic friction and inertia of the actuator-sensor system can be found in Figures B.9 until B.14. The maximum allowed force due to inertia and dynamic friction is 0.1 N each. In the 95% interval the maximum effective inertia is $1.87 \cdot 10^{-4}\,\mathrm{kgm}^2$ and the maximum dynamic friction coefficient is $1.44 \cdot 10^{-3}\,\frac{\mathrm{Nm}}{rad/\mathrm{s}}$ as can be read in the figures.

B.4 Sensor resolution

As was the case with the force computations in Appendix B.2.2, to determine the maximum allowable movement of the actuator/sensor part direct fingertip displacement load-cases are not useful. Therefore a multidimensional volume will be defined in the actuator-angle coordinates. This volume will be converted to the end-effector space where a largest deviation from the neutral position of one of the fingertips will define the limiting end-effector motion. The basics of this method can be found in [Mer06].

The computation starts with defining an input motion range for the actuators. All possible unit displacement combinations of the actuators are, just as in Section B.2.2, the $2^5 = 32$ combinations. In this case displacements instead of forces will be applied, so that it is not self-evident that linearity of the transfer is valid. If large displacements occur the Jacobian matrix will also change. Therefore results using this Jacobian will then be invalid. The used

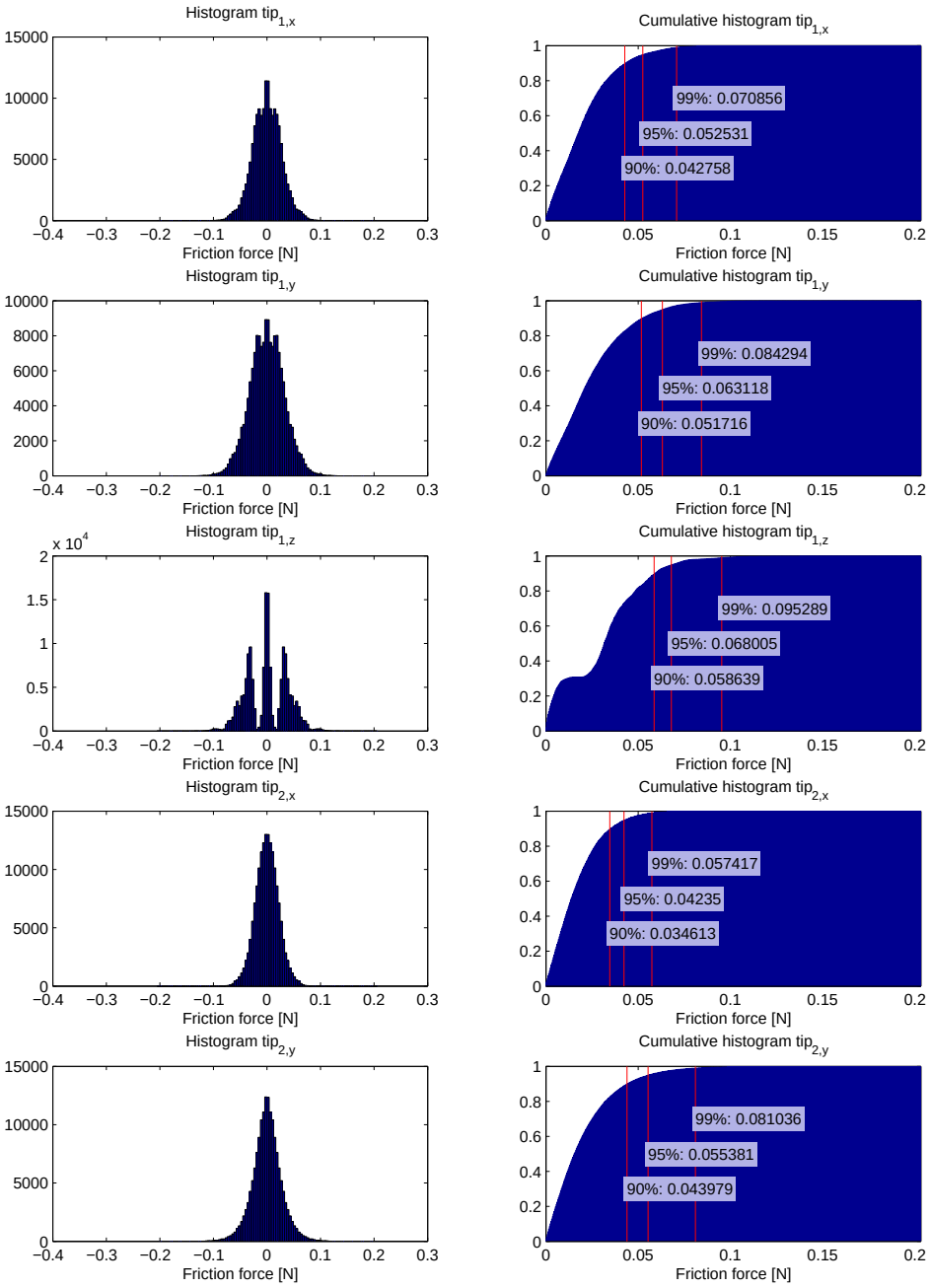

Figure B.10: Dynamic friction force distribution in fingertip coordinates using the dynamic friction coefficient of $1.44{\cdot}10^{-3}\ \frac{\mathrm{Nm}}{rad/\mathrm{s}}$. To determine the cumulative histogram first the absolute values have been taken.

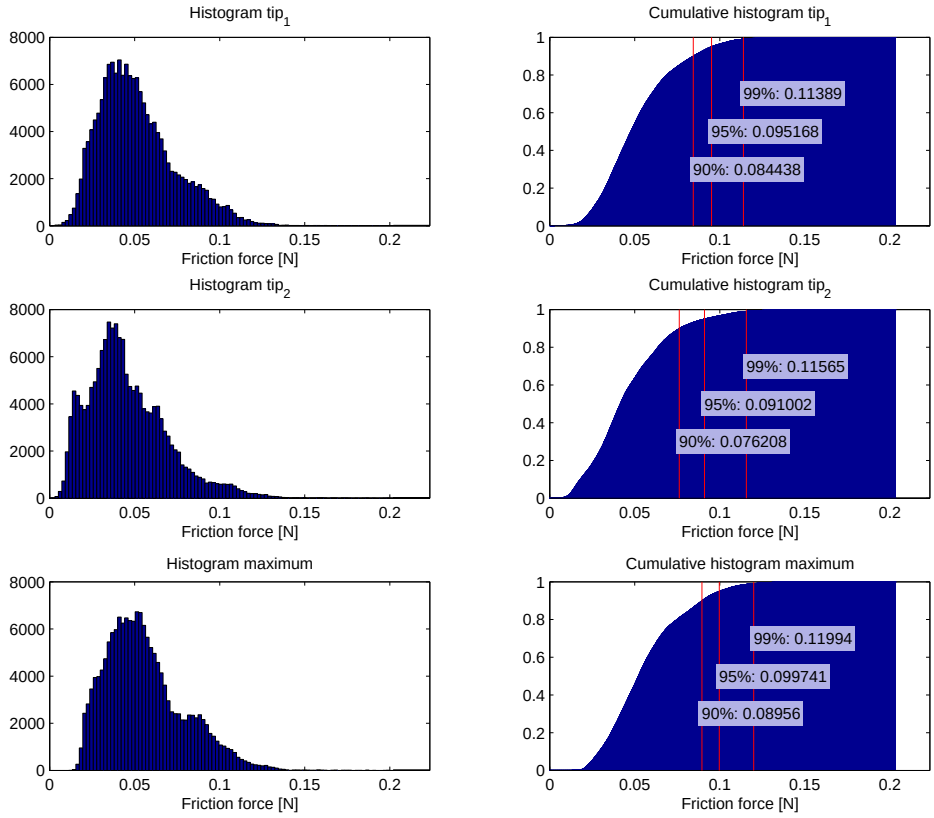

Figure B.11: Magnitude of the dynamic friction force at the fingertips using the dynamic friction coefficient of $1.44 \cdot 10^{-3} \frac{\mathrm{Nm}}{rad/\mathrm{s}}$.

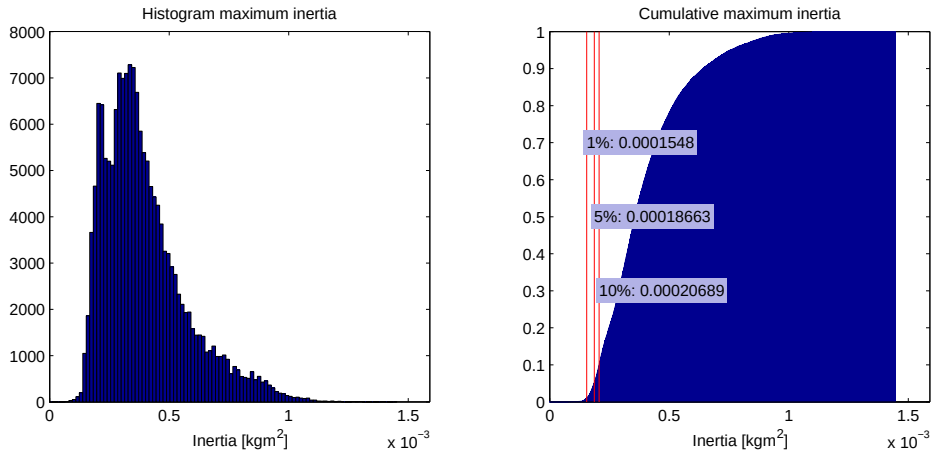

Figure B.12: Maximum allowed motor inertia.

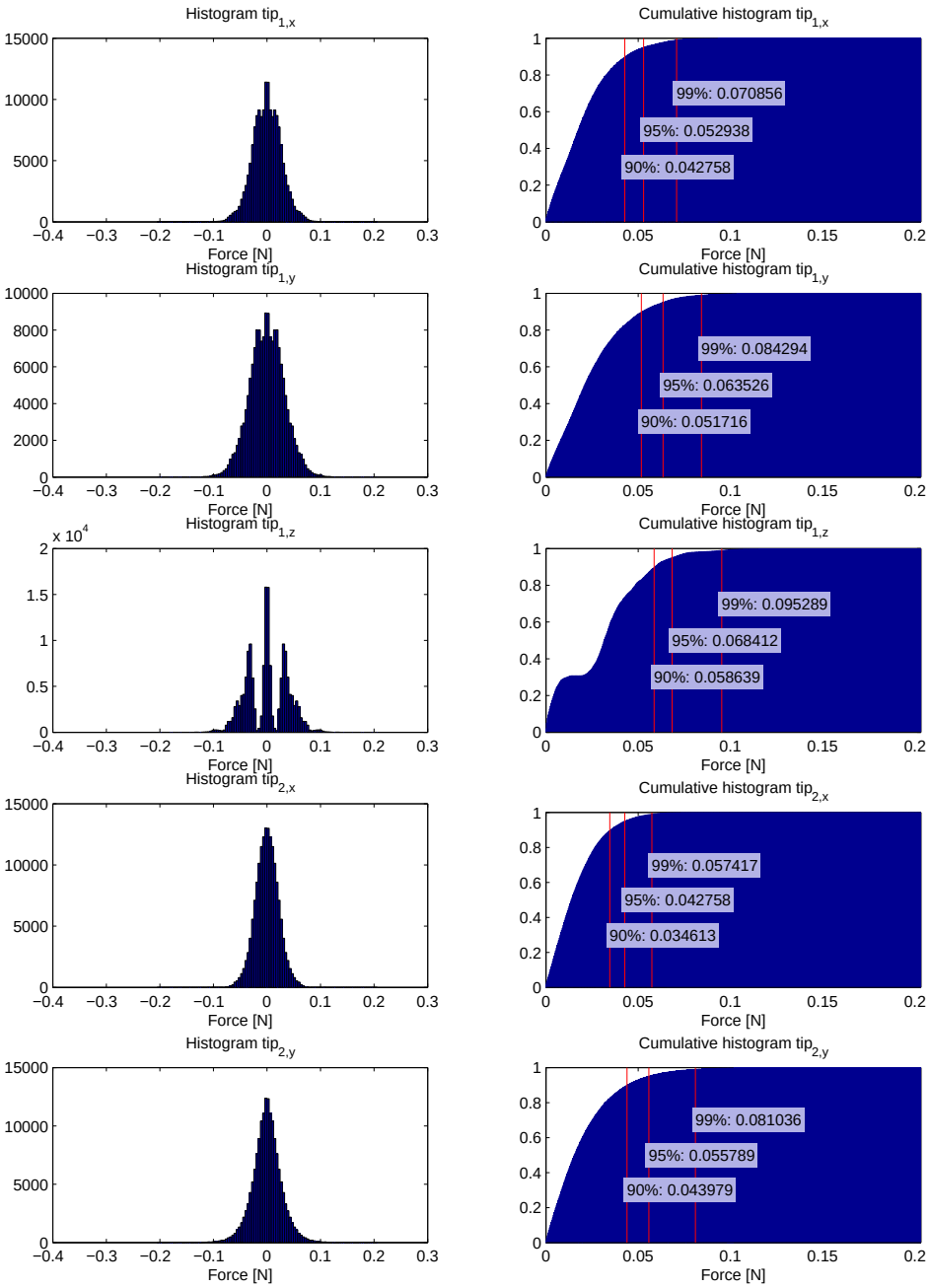

Figure B.13: Inertia force distribution in fingertip coordinates using the maximum effective inertia of $1.87 \cdot 10^{-4}\,\mathrm{kgm}^2$. To determine the cumulative histogram first the absolute values have been taken.

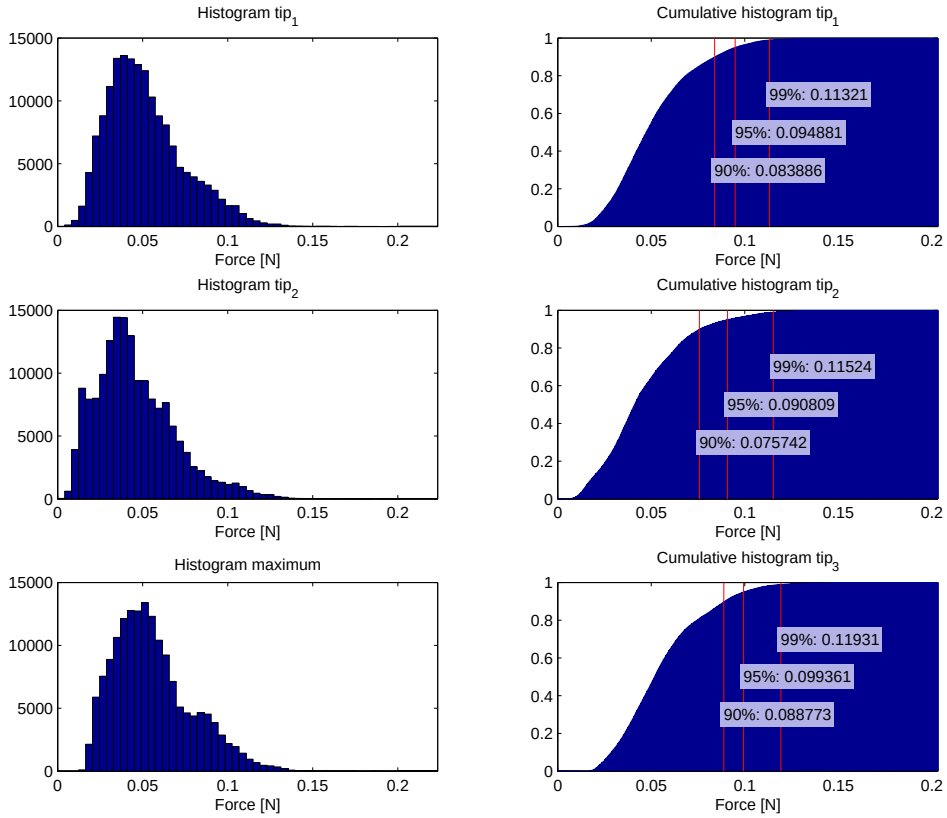

Figure B.14: Magnitude of the inertia force at the fingertips using the maximum effective inertia of $1.87 \cdot 10^{-4}\,\mathrm{kgm}^2$.

basic equation is the description of the velocity relation from Section 2.2:

$$\begin{aligned} \dot{\boldsymbol{\chi}} &= \mathbf{J}\dot{\boldsymbol{q}} \\ \frac{d\boldsymbol{\chi}}{dt} &= \mathbf{J}\frac{d\boldsymbol{q}}{dt} \\ d\boldsymbol{\chi} &= \mathbf{J}d\boldsymbol{q} \end{aligned}$$

as long as dt is not equal to 0. This means that this relation will be used to evaluate the effect of small deviations of $\boldsymbol{q}$ on $\boldsymbol{\chi}$. Since the displacements are now small the computation with the Jacobian, which is in fact a linearization, may be used. As an alternative the forward kinematics could be directly used. This is done to verify the results, but when doing multiple computations using the Jacobian is faster. The reason for this is that the direct equation is not known at the present so that an iterative and therefore relatively slow solution must be used. Note that the iteration also uses the mentioned Jacobian relation to converge to the right solution. More information on this algorithm is available in Appendix E.3.

Now that the end-effector displacement $d\boldsymbol{\chi}$ is known, it must then be evaluated in relation to the defined specifications. This means translating the displacement in general end-effector coordinates $\boldsymbol{\chi}$ to fingertip coordinates $\boldsymbol{\chi}_{tip}$ using the coordinate system equations discussed in [vdVV11]. The largest magnitude of the displacement of both tips is then leading to determine the needed sensor resolution:

$$d\chi_{\max} = \max\left(\left|d\boldsymbol{\chi}_{\text{tip1}}\right|, \left|d\boldsymbol{\chi}_{\text{tip2}}\right|\right)$$

then

$$dq_{\max} = \frac{d\chi_{\text{tip,spec}}}{d\chi_{\max}}$$

because a unit angle dq has been used. When this is evaluated for all displacement cases, on a rectangular grid in space the distribution of the required sensor resolution can be depicted as in Figure B.15. When the 5% limit of the maximum of both tips is used, Figure B.16 shows the distribution of fingertip displacements.

B.5 Position-force coupling

Because an error in the position measurement leads to an error in the Jacobian matrix and thus in the force transfer computation, there will be a coupling between position accuracy and force accuracy. Some first attempts have been made to quantify this effect, however no reliable results have been obtained yet.

The idea is based on the definition of the Jacobian and its inverse:

$$\mathbf{J} = \frac{\partial \boldsymbol{\chi}}{\partial \boldsymbol{q}} = \begin{bmatrix} \frac{\partial x}{\partial q_1} & \cdots & \frac{\partial x}{\partial q_5} \\ \vdots & & \vdots \\ \frac{\partial \rho}{\partial q_1} & \cdots & \frac{\partial \rho}{\partial q_5} \end{bmatrix}$$

$$\mathbf{J}^{-1} = \frac{\partial \boldsymbol{q}}{\partial \boldsymbol{\chi}} = \begin{bmatrix} \frac{\partial q_1}{\partial \chi_1} & \cdots & \frac{\partial q_1}{\partial \chi_5} \\ \vdots & & \vdots \\ \frac{\partial q_5}{\partial \chi_1} & \cdots & \frac{\partial q_5}{\partial \chi_5} \end{bmatrix}$$

The internal torque computation based on the required feedback force is based on Equation (2.4), which contains $\mathbf{J}$. To derive how this depends on a position measurement error, the derivative of $\mathbf{J}$ to $\boldsymbol{q}$ has to be evaluated:

$$\frac{\partial \mathbf{J}}{\partial \boldsymbol{q}} = \frac{\partial^2 \boldsymbol{\chi}}{\partial \boldsymbol{q} \partial \boldsymbol{q}}$$

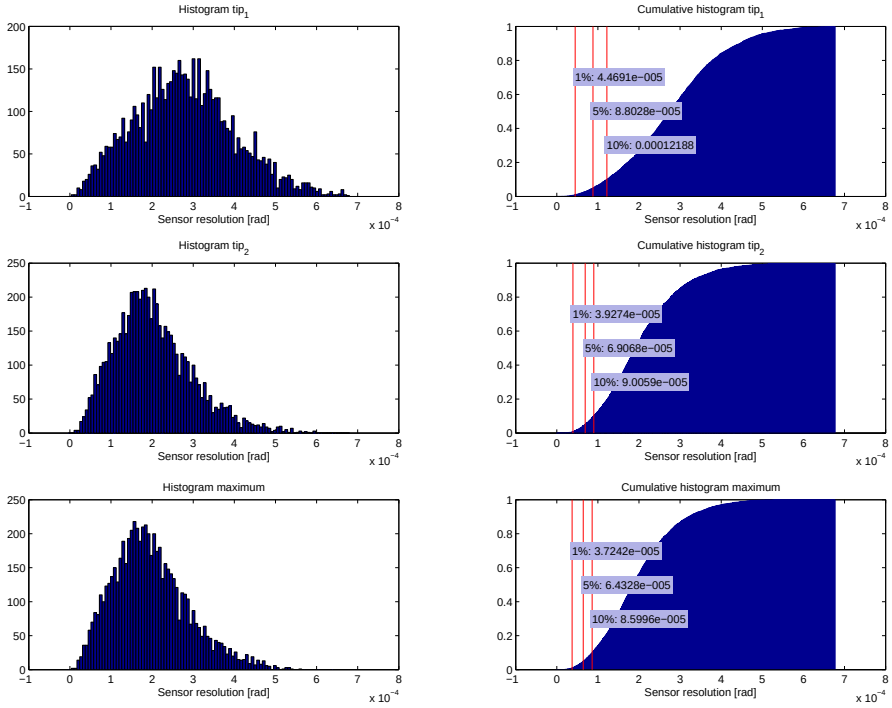

Figure B.15: Required sensor resolution. The most limiting displacement case, the one that resulted in the smallest sensor resolution is depicted. The results are obtained from a 7 step grid in 5 dimensions. From top to bottom the graphs give the limits of tip 1, tip 2 and the maximum of both where the maximum is the sensor resolution resulting from the maximum tip displacement. The left row is the histogram, the right row is cumulative.

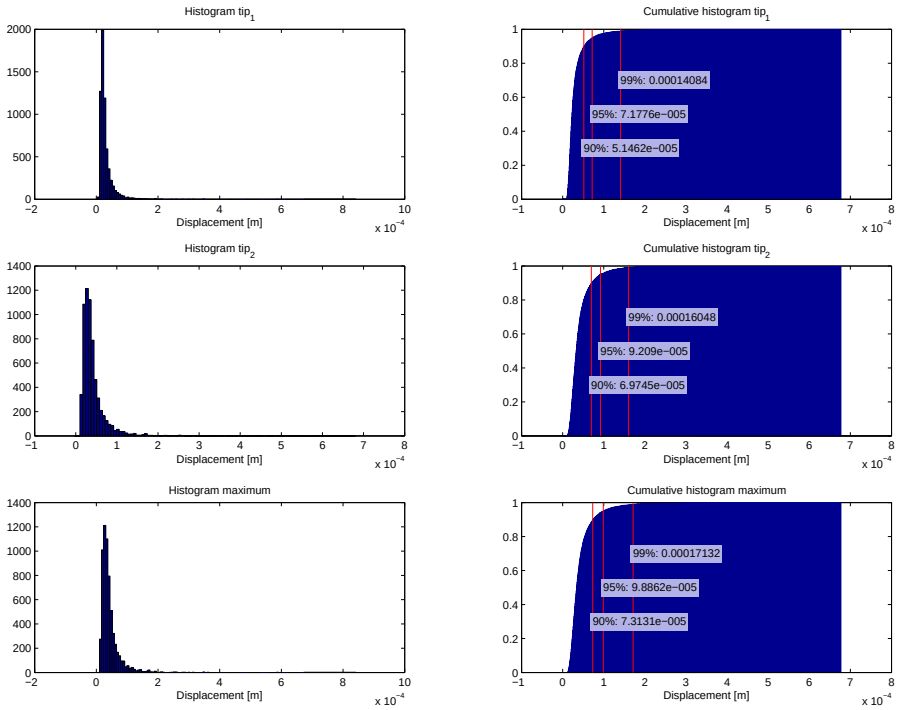

Figure B.16: Fingertip displacements when actuator displacements of $6.4 \cdot 10^{-5}\,\mathrm{rad}$ are allowed.

With this second derivative the coupling effect should be computed. In the current mechanism it may be assumed that the Jacobian is rather smooth in space and therefore this effect can be neglected.

B.6 Distribution of extremities

In Figures B.17 and B.18 an overview is given of the locations of the evaluated points in the robot workspace that are outside the 95% interval and thus contain the 5% highest forces and the 5% smallest resolutions. Because of the nature with which these quantities are evaluated the results are very similar. The Equations to evaluate accuracy (2.1) and force (2.4) both evaluate the Jacobian (or the transpose), but not the inverse. The differences only result from the difference in the applied force and displacement load-cases. The most obvious relation is found in the end-effector grasping angle θ, where almost all extremities lie at extreme angles. Therefore limiting the grasping angle θ will result in a significant decrease in the required maximum actuator torques and sensor resolution. Also large actuator angles seem to contain more extremities.

However when observing all accuracies as a function of actuator angle in Figure B.19 it appears that the actuator angle relation described before does not hold for all points, but only for the extremities. Another notable point is the significant difference in the motor-motions corresponding to different tip motion directions. This can however be explained easily by the fact that motor 3 is directly connected to tip 1 and motor 1 and 5 are directly connected to tip 2. Note that because the evaluation method for maximum force and sensor resolution are quite comparable, the results in Figure B.19 can also be evaluated in terms of force. This can be imagined by considering that the power should be in balance on both sides of the mechanism:

$$\boldsymbol{F}^T \dot{\boldsymbol{\chi}} = \boldsymbol{\tau}^T \dot{\boldsymbol{q}}$$
$$\boldsymbol{F}^T d\boldsymbol{\chi} = \boldsymbol{\tau}^T d\boldsymbol{q}$$

when dt is unequal to 0.

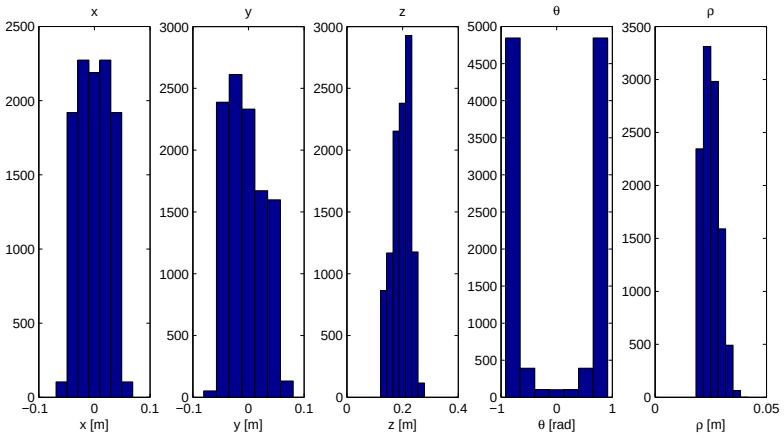

(a) χ coordinates.

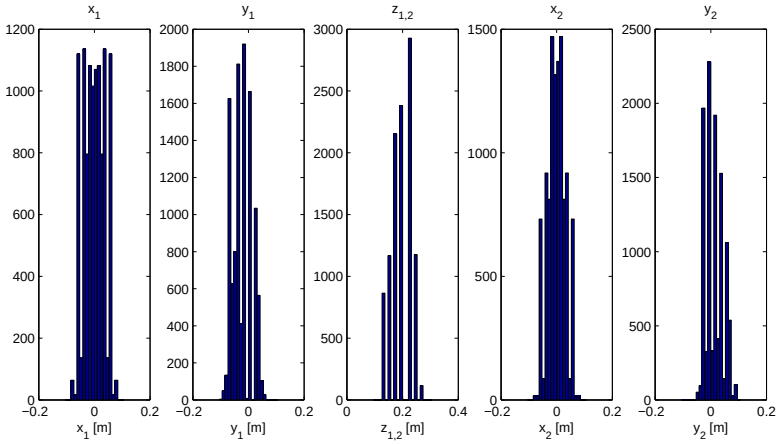

(b) χ_{tip} coordinates.

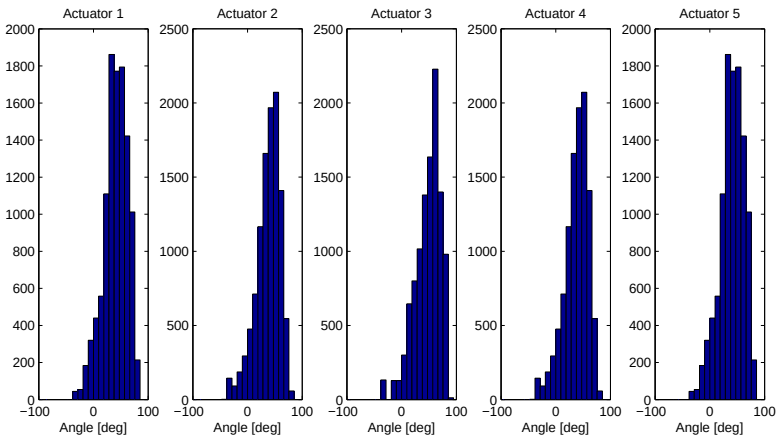

(c) $\boldsymbol{q}$ (motor angle) coordinates.

Figure B.17: Locations of the top 5% highest forces

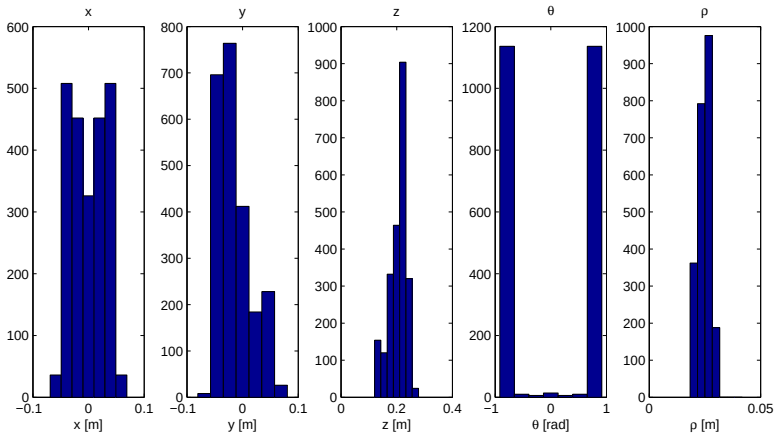

(a) χ coordinates.

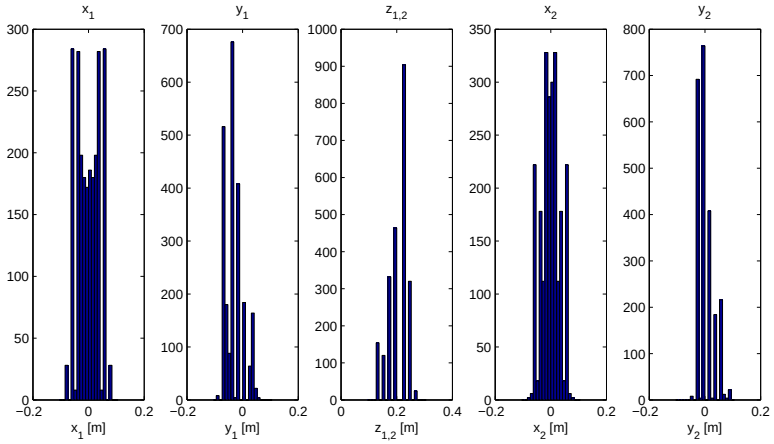

(b) χ_{tip} coordinates.

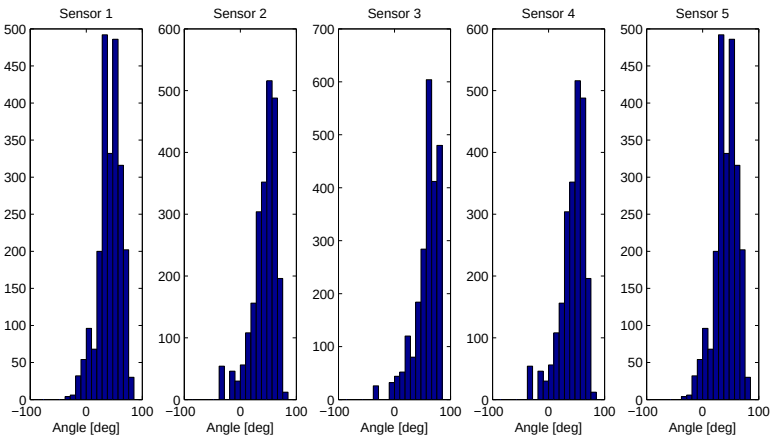

(c) $\boldsymbol{q}$ (motor angle) coordinates.

Figure B.18: Locations of the top 5% smallest resolutions.

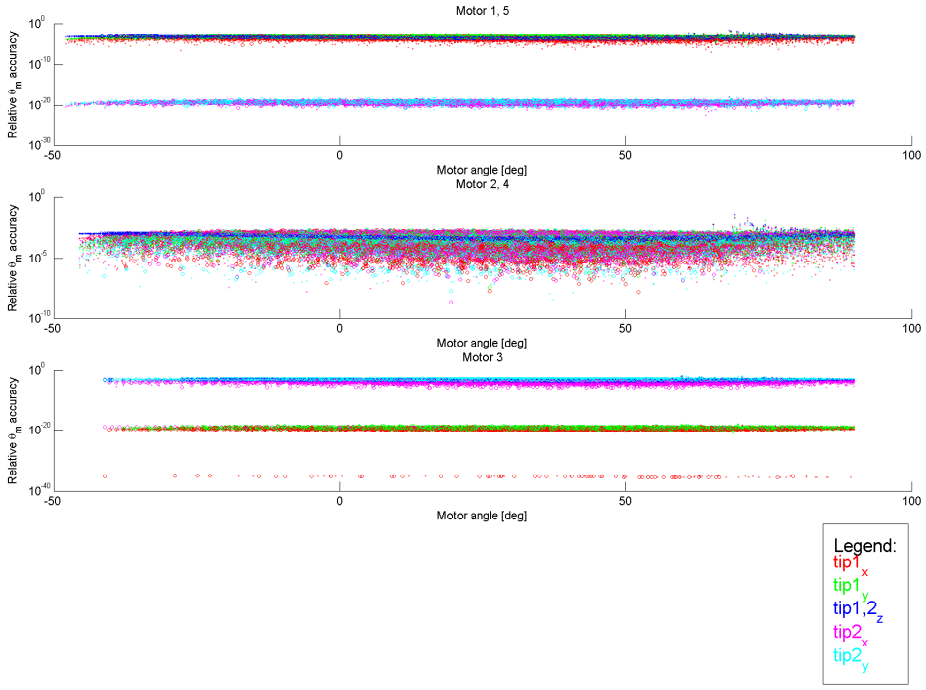

Figure B.19: Distribution of sensor accuracy as a function of sensor position. Points in the workspace are drawn with a circle, the other points are a dot. The points are colored according to the motion direction they represent. The points on the graph represent the motor angle displacement corresponding to a 0.1 mm end-effector motion in the given directions.

Appendix C

Conceptual design

Since a rotational motion and force is required, one of the obvious solutions is the use of a standard electric rotational drive and a rotational encoder. However there are other solutions possible that will be treated further on. All solutions can be combined out of 2 reasonably separable choices: (1) The type of transmission between the actual actuator or sensor and the robot, discussed in Appendix C.1, and (2) the type of the actuator or sensor itself, discussed in Appendices C.2 and C.3.

C.1 Transmission options

Using a transmission between the actuator/sensor and the robot is quite a common drive and measurement method, as it can be found on commercial haptic interfaces such as the Novint Falcon [Nov11] and the Force Dimension Omega series [Dim11]. Using a large transmission allows the use of small electric motors to keep the design relatively cheap.

Using a transmission in the drive train of a haptic device puts some special attention to a number of requirements. These will be evaluated for a number of possible transmission options. First of all play in the transmission must be eliminated. When a mechanism experiences play there is no direct connection between the actuator and the rest of the robot when the actuator changes both motion and force direction. The actuator will then accelerate due to the lack of counterforce from the robot until it reaches the end of the play. Then the actuator decelerates again due to the reaction forces from the robot. This means that play introduces unwanted abrupt force changes. Also other unwanted parasitic forces such as friction should be minimized in the transmission since they distort the force feedback and result into power loss. Next the properties of a number of transmission types will be evaluated.

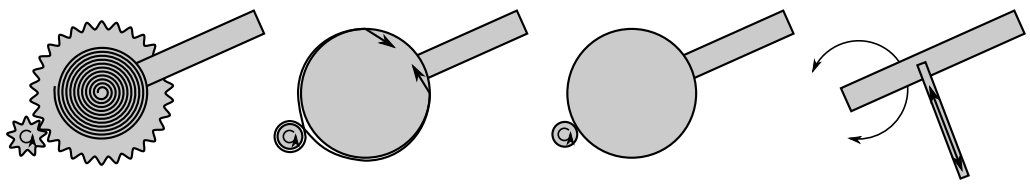

Figure C.1: Overview of the reviewed transmission options. From left to right: preloaded gears, cable, friction wheel and mechanism transmissions.

C.1.1 Gear

Gear transmissions are often a standard option on commercially available electric actuators and are therefore widely used. An inherent problem of a gear transmission is however play due to the finite distance that has to exist between the teeth of a gear system and friction. [Kos05] suggest using a preload to prevent changes of load direction and by that play. This means however that a preload larger than the maximum expected force should be continuously present. The preload should be applied at the end of the drive train, which would mean in the case of this mechanism at the lower limb and optionally at the motor. When applying one preload, the motor has to deliver the preload torque as well as the useful torque. With the preload applied on both sides the preload forces should match very precisely to avoid that preload forces reach the user. Adding a preload also increases the friction in the sliding contact between the teeth. Due to the increased contact force more power is dissipated because the friction force is increased.

C.1.2 Cable and band

Cable transmissions are widely used in commercial haptic devices [Dim11, Nov11] and more experimental setups. This is due to the easy way in which play can be eliminated by applying pretension. Friction can however not be eliminated totally, the bending radius of the cable changes causing slip between the cable and the disk.

C.1.3 Friction

Friction wheels could be used to transmit torque from the motor to the lower limb. When high torques must be transmitted, the force pressing the friction wheels together must also be significantly high. Also there is no easy means to prevent slip between the friction wheels. This might especially be a problem when a position measurement has to be done through the transmission.

C.1.4 Mechanism

Using a mechanism to transmit forces to the robot might be particularly interesting when a linear force actuator is used as motor. Using a mechanism as a rotation to rotation transmission would mean that only small rotations could be used, which is not desirable with the PentaGriph mechanism. Therefore using a mechanism to convert linear into rotational motion is probably more useful. Section B.6 shows that the extreme forces and sensor accuracies are concentrated around specific actuator angles but, on average the resolution and force distribution does not significantly change as a function of the actuator angle. Therefore using a mechanism as a transmission has no significant advantage.

C.2 Actuator concepts

In this section a number of actuators that could be used with or without a transmission will be discussed. The focus will be on electromagnetic actuator because their characteristics make it relatively easy to control the exerted torque. Other options like pneumatic actuation are more suitable for position control and suffer from significant parasitic forces because their nature is more contact-based.

C.2.1 Rotational electromagnetic drive

In [Com00] a comprehensive overview of the available types of electromagnetic rotational drives is given. The following types will be considered:

- Brushed motors
  - Iron armature
  - Hollow rotor
  - Disk armature
- Brushless motors (electronic commutation)

In the application of a haptic drive the main importance is to combine minimum inertia and other parasitic forces such as friction and cogging while obtaining a maximum peak output torque. Therefore actuators such as stepper motors will not be considered.

In terms of parasitic forces the hollow rotor and disk armature would be recommended due to their light iron-less rotor. The possible torques are however limited for these forms. In electronically commutated motors the windings are not in the rotor but in the stator, allowing larger currents and thus larger torques. Also the use of brushes for mechanical commutation creates electrical limitations and increased friction, which can be avoided by using brushless motors. Finally brushless motors can be used in the same position for longer time without damage, which might very well occur in the current application.

C.2.2 Torque motor

A solution that seemed to fit very nice with the characteristics of the specified actuation is the torque motor, also known as limited angle torque actuator. This electromagnetic type actuator is designed to exert torques in the same actuator position for longer periods of time an is more frequently used in force-feedback systems [Wik11].

Gathering information from manufacturers like [HT11, SMT10] it appears however that in general the inertia of these torque motors is relatively large compared to brushless for instance DC motors. Also the total stroke of the actuator is often limited to angles like 100° or 150°, so that custom wiring or an entire custom design is needed.

C.2.3 Force control system

To overcome the problem of parasitic forces from the actuator system to a large extent, a force control system can be constructed. The idea behind such a system is that most of these unwanted forces can be eliminated by measuring the actually exerted load and controlling the actuator torque such that the torque error goes to zero.

When designing such a force control system the first main choice is the location of the force sensor. This can be either at the lower limb (between the actuator system and the robot) or at the fingertips (between the robot and the user). These options will be considered in the following Sections.

C.2.3.1 Actuator torque measurement

By using a torque measurement at the actuator system a local force control loop can be created that keeps the net torque to the lower limb at the required value. Also at a zero requested force this will make sure that the actuator itself will overcome parasitic friction and inertial forces. This could reduce the effective inertia of the actuator system to zero, however the inertia of the part of the load cell that is rigidly connected to the lower limb. A suitable torque sensor is the Futek TFF325 [FAST10] which has an estimated inertia in the order of $10^{-6}\,\mathrm{kgm}^2$, an order of magnitude lower than the selected actuator.

Important disadvantages of this system are the increased complexity of the system and the need to make a separate suspension for the lower limb, because it is not placed directly on the motor suspension and the suspension loads should not be lead through the load cell.

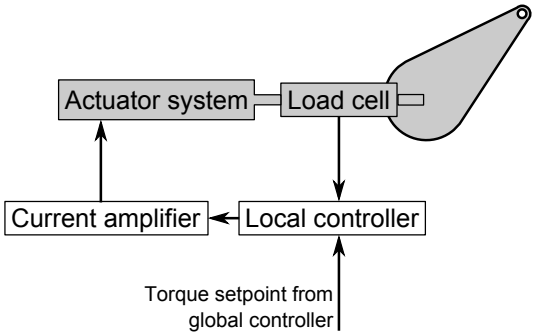

Figure C.2: Setup of the force control system with actuator torque measurement.

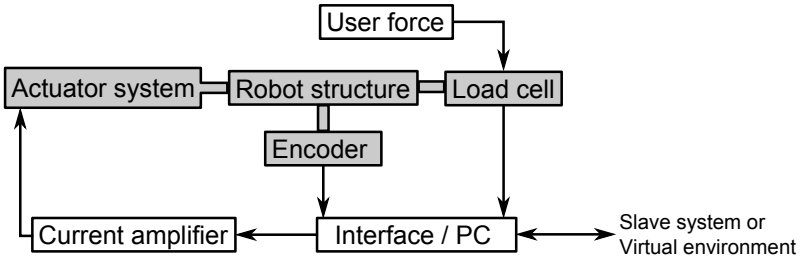

Figure C.3: Setup of the force control system with user force measurement.

C.2.3.2 User force measurement

A somewhat more advanced version of the force control loop system measures the force that is exerted to the user. This configuration might look like a 4-channel controlled haptic system, but in this case the measured force is only used locally in the master device and not necessarily communicated to the slave. Because the force is controlled at the fingertip of the robot, the controller also needs to have information about the force transfer from the actuators to the fingertips. Therefore this controller will be embedded in the global controller of the master, since that information is already available there. The structure of the control system will then be somewhat adapted, as is depicted in Figure C.4. The added force controller block is elaborated in Figure C.5. In this block the requested force is sent feedforward to the output. With force measurement implemented a feedback loop controls the difference

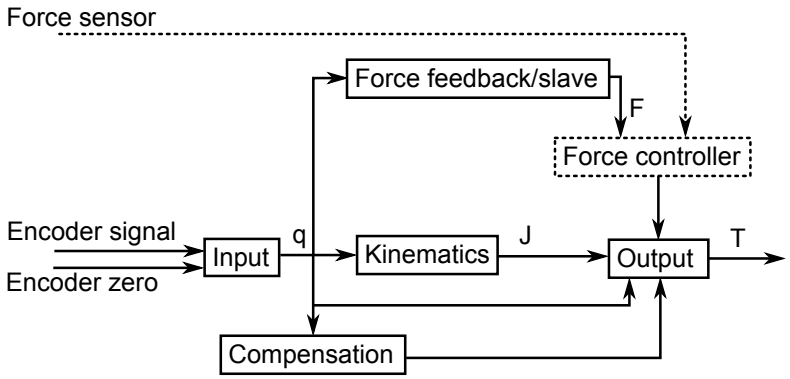

Figure C.4: Schematic overview of the software structure when force control with measurement at the fingertip will be implemented. This is the content of the Interface / PC block in Figure 3.2. The dashed elements are added compared to the general schematic (Figure 3.3).

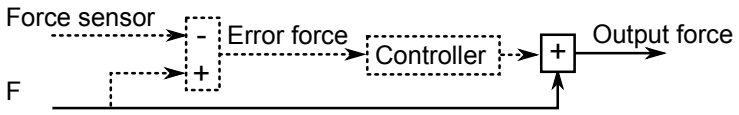

Figure C.5: Schematic overview of the force controller stage. This is the content of the Force controller block in Figure 3.3.

between the measured and the requested force and adds that to the output.

A major advantage of this system is that not only parasitic forces resulting from the actuator and sensor system can be compensated, but also friction and inertia of the structure. The disadvantage is however that a force sensor has to be placed at the top of the robot and thus increasing the inertia. This will however also be partly compensated by the system itself. Also the control of this system will have some advanced problems due to the position dependent stiffness, damping and inertia of the system.

Force sensor Since force measurement takes place at the fingertips the sensors need to measure the user forces in 3 Cartesian coordinates per fingertip. Such strain gauge based sensors are available, but requires a complex readout system with a price in the order of € 10^4. An alternative is a force sensitive foil solution. These sensors contain a force sensitive resistor that can be read out using an op-amp circuit. [Tek10] shows that the conductivity is approximately proportional to the applied force giving decreased resistance sensitivity at higher forces. These sensors are cheap and give the required range and accuracy for human finger force measurement. By placing this foil sensor in a custom designed ring, the measurement can be integrated in the fingertips.

Two examples of these foil based sensor manufacturers are Interlink Electronics [Tec10] and Tekscan [Tek10]. A conceptual design using the Interlink FSR 400 and FSR 402 is given in Figure C.6. This design places two force sensors opposite to each other in x and y directions, so that forces in both directions can be measured. This also gives the opportunity of placing them in a bridge circuit to linearize the output. Based on available data of the used sensor the final transfer has been simulated and is given in Figure C.7. The bridge places the two sensors electrically in series. A constant voltage (in the figure 10 V) is applied over the bridge and the voltage on the connection between the sensors is given.

C.2.4 Dual stage actuator

The Dual stage actuator concept is based on the paper [MHRH09]. The main idea is that to reduce the effective inertia that is felt by the user a 2 stage actuator should be used: A small and light actuator connected directly to the user and a larger actuator connected through a viscous damper, in this case an eddy current damper. Due to this decoupling it would still be possible to exert large forces, but the inertia would be decoupled.

To make a first analysis of this concept the eddy current system including the large motor has been modeled. This analysis might also be usefull for evaluating other concepts based on eddy currents. A sketch of the model is depicted in Figure C.8.

The magnetic circuit The following magnetic circuit analysis assumes the system to be at rest. The permanent magnet (PM) has a remanent magnetic field B_r and a relative permeability of μ_m. This means that:

$$H_\mathrm{c} = -\frac{B_\mathrm{r}}{\mu_\mathrm{m}}$$

(This assumes a zero-reluctance circuit around the magnet. H_c is independent of the circuit reluctance.) This means the equivalent magnetomotive force (MMF) of the PM is:

$$\mathcal{F} = -H_\mathrm{c} l_\mathrm{m}$$

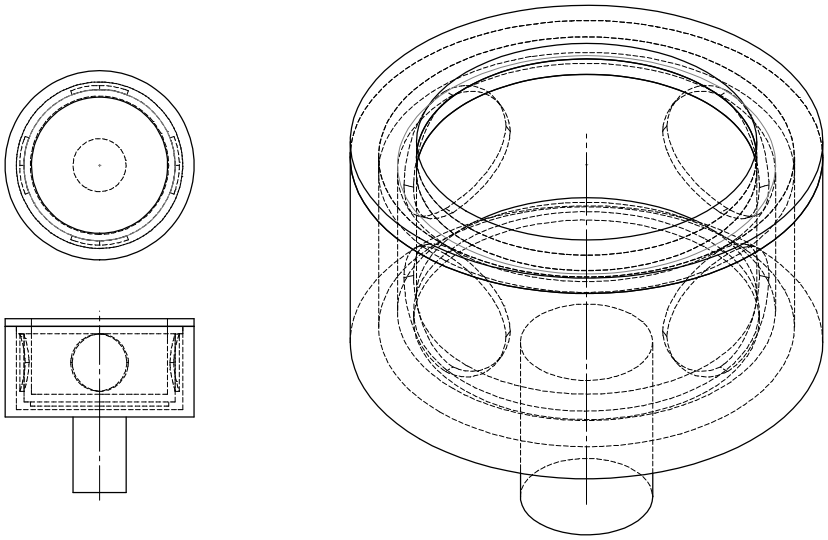

Figure C.6: Conceptual design of a fingertip force sensor based on foil sensors. In x-y direction two sensors are opposite to each other, in z-direction a ring-shaped spring is used as preload. Also other configurations with a double z-sensor are possible. Further some decoupling between force-direction might be required.

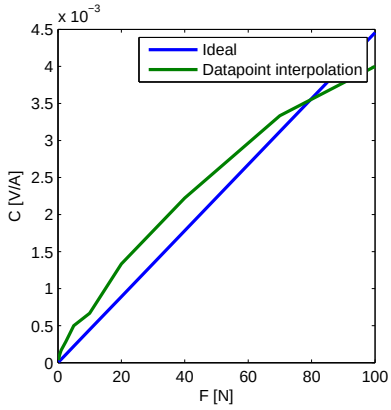

(a) Single force sensor characteristic.

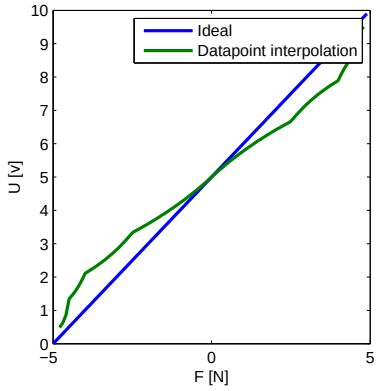

(b) Bridge configuration characteristic.

Figure C.7: Output characteristic of a foil force sensor bridge. Based on the conductivity data of the FSR 400/FSR 402, available from [Tec10].

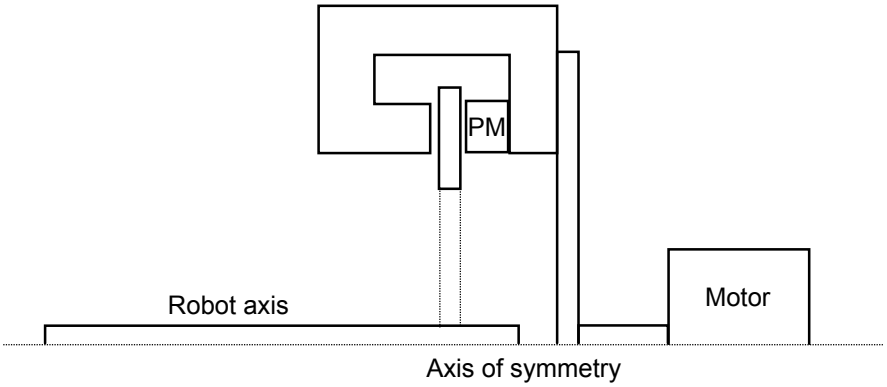

Figure C.8: Eddy current damper driven actuator setup sketch.

with l_{m} is the length of the magnet. The total circuit reluctance is:

$$\Re_{\mathrm{tot}} = \sum_n \Re_n = \Re_{\mathrm{m}} + \Re_{\mathrm{c}} + \Re_{\mathrm{g}} + \Re_{\mathrm{d}}$$

where the subscripts are: m for magnet, c for core, g for air gap and d for disk. The reluctance of a part is given by: $\Re = \frac{l}{A\mu}$. The flux through the entire circuit is constant:

$$\phi = \frac{\mathcal{F}}{\Re_{\mathrm{tot}}} = \frac{-H_{\mathrm{c}} l_{\mathrm{m}}}{\Re_{\mathrm{m}} + \Re_{\mathrm{c}} + \Re_{\mathrm{g}} + \Re_{\mathrm{d}}}$$

or

$$\begin{aligned} \overline{B} = \frac{\phi}{A} = \frac{\mathcal{F}}{\Re_{\mathrm{tot}} A} &= \frac{-H_{\mathrm{c}} l_{\mathrm{m}}}{\left(\Re_{\mathrm{m}} + \Re_{\mathrm{c}} + \Re_{\mathrm{g}} + \Re_{\mathrm{d}}\right) A} \\ &= \frac{-H_c l_m}{\left(\frac{l_{\mathrm{m}}}{A_{\mathrm{m}}\mu_{\mathrm{m}}} + \frac{l_{\mathrm{c}}}{A_{\mathrm{c}}\mu_{\mathrm{c}}} + \frac{l_{\mathrm{g}}}{A_{\mathrm{g}}\mu_{\mathrm{g}}} + \frac{l_{\mathrm{d}}}{A_{\mathrm{d}}\mu_{\mathrm{d}}}\right) A} \end{aligned}$$

Eddy currents The ring has a conductivity σ_{d}. The volume of the disk subjected to the magnetic field (thus where eddy currents will occur) is $V_{\mathrm{d}} = A_{\mathrm{d}} l_{\mathrm{d}}$. Then the eddy current damping force can be estimated as in [EKG09] that states:

$$\boldsymbol{F} = \int_{\Gamma} \boldsymbol{J} \times \boldsymbol{B} d\Gamma$$

with

$$\boldsymbol{J} = \sigma \left(\boldsymbol{v} \times \boldsymbol{B}\right)$$

the current density and Γ the volume. By assuming speed $\boldsymbol{v}$ and field $\boldsymbol{B}$ constant and orthogonal to each other it enables scalarizing to:

$$F = V_{\mathrm{d}} \sigma_{\mathrm{d}} v \overline{B}^2$$

resulting in a linear damping coefficient of:

$$c_{\mathrm{lin}} = \frac{F}{v} = \frac{V_{\mathrm{d}} \sigma_{\mathrm{d}} v \overline{B}^2}{v} = V_{\mathrm{d}} \sigma_{\mathrm{d}} \overline{B}^2$$

If now n dampers are on the circumference of the disk, the rotational damping-coefficient is:

$$c_{\mathrm{rot}} = \frac{T}{\omega} = \frac{Fr}{\frac{v}{r}} = n c_{\mathrm{lin}} r^2 = n V_{\mathrm{d}} \sigma_{\mathrm{d}} \overline{B}^2 r^2$$

Further evaluation of these equations indicated that the transfer function from the motor current to the output torque shows first order behaviour. Numerical analysis assuming some reasonable values for the system parameters resulted in a time constant in the order of 10^{-2} s.

Discussion The method that determines the eddy currents is quite coarse, but gives a rough indication of the expected behaviour. Creating a changing magnetic field using moving permanent magnets however seems to be a relatively difficult method. By using coils to generate the changing field, much lower time constants can be achieved.

C.2.5 Mechanical brake

Another type of dual-stage actuator is the mechanical brake actuator. The main assumption behind this concept is that the majority of the forces that the actuator should generate are counteracting the motion of the user or occur at standstill. These forces can then be exerted by accurately controllable brakes. A second stage, consisting of a small electromagnetic actuator, should account for the forces that cannot be exerted in this way.

The main advantage of this concept is that with a relatively light actuator large forces can be exerted. However numerous challenges occur when this concept will be brought into practice. The most important is designing a controllable brake with a very predictable static and dynamic friction behaviour. To achieve this possibly position and force measurement will have to be combined making the system rather complex. Another solution might be to use eddy current braking as is done in [GH08]. There not a rotating permanent magnet, but a stationary coil is used to generate the magnetic field. The system that has to be created for this is however still quite complex. Finally it is not known which part of the force feedback can indeed be generated using braking only.

C.3 Sensor concepts

C.3.1 Rotational encoder

To perform a high resolution rotation measurement a common solution is using an optical rotary encoder. Because the measurement itself is contactless the disturbance forces will be relatively limited. Another type of contactless encoder is the magnetic encoder. They are however relatively expensive and will probably be influenced by the magnetic field produced by the motors. An important choice that has to be made is whether the rotation is directly measured or using a transmission. This will depend on the possibility of achieving a high resolution measurement. For the choice of transmission type the options of Appendix C.1 are open. When a transmission is used an encoder homing system is however necessary. This can be done with a light barrier system. Micrometer accuracy is possible with such systems.

Eliminating the transmission can be beneficial in terms of parasitic forces, because they will not be amplified. However because the encoder must then be more accurate the internal parasitic forces themselves increase, for instance due to a heavier suspension and higher needed internal stiffnesses. The encoder grating could also be directly applied on the lower limb, but due to the needed resolution the suspension of the lower limb and the lower limb itself must be relatively rigid to remain free from internal deformations. By partially decoupling the encoder with a transmission less unwanted forces will influence the position measurement.

C.3.2 Linear encoder

Measuring the rotational motion with a linear encoder and a transmission can be useful when there is a clear position dependent resolution or accuracy needed. From Section C.1.4 it is however known that such a relation is not significant, eliminating the need for this concept.

C.3.3 Reflective

A reflective system bounces a light beam to the lower limb and defines the angle based on the reflected light. This however works best with small angles, which makes it less suitable for this system.

Appendix D

Design details

This Appendix gives additional details about additional calculations and details that have been performed for the design described in Chapter 3.

D.1 Actuator transmission

The following analysis investigates the influence of the transmission ratio on the actuator system performance. Mostly a transmission is used to lower the required motor torque while the motors motion increases. This has however an important disadvantage: also parasitic forces originating inside the motor will be amplified by the transmission. This effect is even more serious when these forces are proportional to the motion of the motor itself, such as viscous friction and inertia. Calling the transmission i, the motor speed $\dot{q}_m$ is defined as:

$$\dot{q}_{\mathrm{m}} = i\dot{q}$$

while the motor torque due to dynamic friction is:

$$\tau_{\mathrm{m}} = c_{\mathrm{m}}\dot{q}_{\mathrm{m}} = ic_{\mathrm{m}}\dot{q}$$

The motor torque will also be amplified with a factor i:

$$\tau = i\tau_{\mathrm{m}} = i^2 c_{\mathrm{m}}\dot{q}$$

In other words: the effective friction coefficient is:

$$c_{\mathrm{eff}} = i^2 c_{\mathrm{m}} \tag{D.1}$$

An analogous reasoning applies to the effective motor inertia:

$$I_{\mathrm{eff}} = i^2 I_{\mathrm{m}} \tag{D.2}$$

To investigate the real influence of the transmission ratio on the effective properties of the actuation system an investigation has been done to properties of real available electric motors. The following motor series have been reviewed:

- Maxon DC motor: RE program (12 samples) [Mot10]
- Maxon EC motor: EC program (8 samples) [Mot10]
- Faulhaber Brushless DC-Servomotors (9 samples) [Fau11]
- SLMTI Brushless High Performance Servo Series (67 samples) [SMT10]

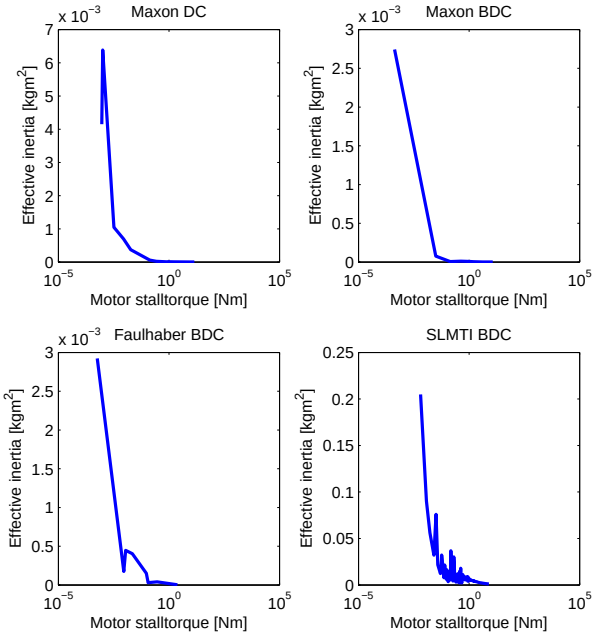

Figure D.1: Comparison of the effective inertia of an actuation system as a function of the motor stall torque.

These series all contain motors that have properties around the right order of magnitude for this specific application. Note that not all 4 datasets are of the same size, the dataset of SLMTI has by far the most different types. Also the information that is available about the different series is not the same.

The analysis that has been done is based on placement of each individual motor in a setup with a transmission. The transmission ratio is defined as the ratio of unity and the motor stall torque, so that the motor with transmission can exert a maximum torque of 1 Nm.

The first analysis has been done with all 4 series of motors: based on the transmission ratio and Equation (D.2) the effective inertia I_{eff} is computed and depicted as a function of the motor stall torque in Figure D.1.

Only for the Faulhaber series additional information on friction was available. Therefore only with these motors the effective dynamic friction coefficient and the effective static friction torque have been computed and depicted in Figure D.2

Finally for the Maxon DC series, also the price given on their website has been analyzed, to obtain information about the cost of low effective inertia. This is depicted in Figure D.3.

Observing the results it can first of all be stated that there is a significant relation between the maximum torque an electric motor can generate and the effective inertia of the actuation system. In all series it is visible that choosing a larger motor will in the end lead to a smaller effective inertia. Also the dynamic and the static friction, the last of which is only dependent on i, while the other quantities depend on i^2, give a clear trend towards smaller disturbance torques when using a small transmission ratio. Decreasing the friction and inertia by using larger actuators might however significantly increase the system cost as can be seen in Figure D.3.

The graphs in Figures D.1, D.2 and D.3 are however not completely monotonous. Outliers might originate from the items within a series being different from each other in more than one way. Not all items where for instance available with the same nominal voltage rating. As much as possible comparable ratings have been used, but this was not possible in all cases. Also some items may be designed with a different intent, causing the results to deviate. The

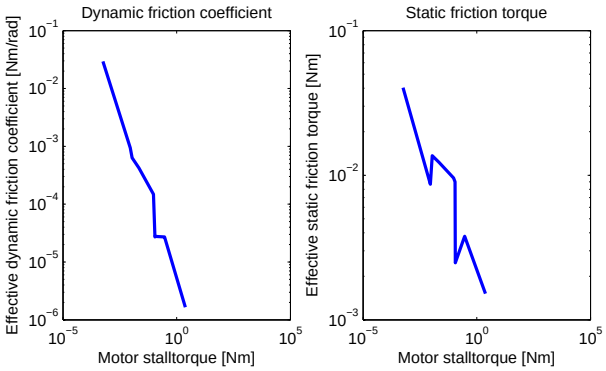

Figure D.2: Effective friction properties versus the motor stall torque.

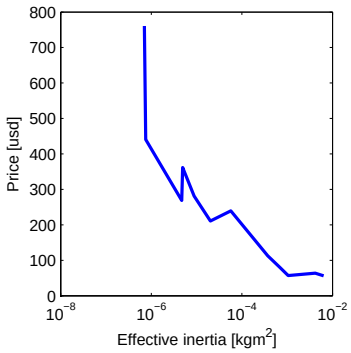

Figure D.3: Cost of a motor versus the effective inertia of the system.

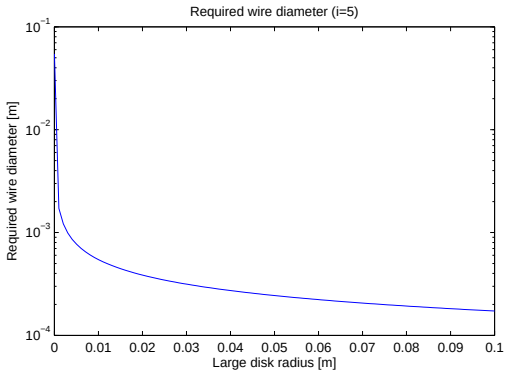

Figure D.4: Required wire diameter as a function of the radius of the large transmission disk.

main trend remains however clear: to minimize the friction and inertia torques a high torque motor and a low transmission ratio should be used.

D.2 Encoder transmission

Because the inertia and dynamic friction of encoders is much more limited, the encoder transmission is expected to be less critical. The following will focus on the wire used in the encoder transmission.

The internal force in the wire depends on the radii of the disk over which they run. The encoder torque is determined by two factors: the inertia and the static friction. The inertia is composed of the encoder and the wire bus inertia, the friction comes from the encoder. By assuming that the wire runs over $360°$ of the large disk (the lower limb) and that the wire deformation difference between plus and minus the maximum expected force should remain within the accuracy, a minimum steel wire thickness of 0.4 mm is needed. Figure D.4 shows the relation between the wire diameter required to limit the angular position error due to wire elongation as a function of the radius of the large transmission disk. Using a small safety margin 0.5 mm steel wire will be selected. The inertia of the cable is negligible as can be seen in Appendix D.12.

The maximum force found for a 25 mm large disk radius is 2 N (caused by the static friction). The preload applied to the wire with springs should thus be at least this value. Because a too low preload should be avoided a large safety margin should be applied. Therefore a preload of 10 N will be used.

D.3 Lower limb

The required stiffness at the end of the lower limb, defined by [Vog11] is $3.6 \cdot 10^5 \frac{\mathrm{N}}{\mathrm{m}}$, while maximum loads are in the order of 30 N in actuation direction and 10 N perpendicular to that. The stiffness has been verified in [Vog11]. To improve the stiffness a closed structure will be created by closing the limb with a plate, showed in Figure D.5.

In order to guide the steel wire and hold the spring, holes are drilled in the sides which will contain pins or hooks for this purpose. The lower limb will be connected to the motor flange using 3 bolts. Other considered options for this connection are conical and clamping structures inspired on examples in [DM05], however implementing these connection types in the lower limb appeared to impose too much structural demands on the lower limb that would compromise the other functions.

Figure D.5: Lower limb pictures. In the upper picture the inner structure is clearly visible. In the lower picture also the cover plate is shown.

D.4 Motor flange

The main function of the motor flange is to make the lower limb detachable from the motor. The flange is glued on the motor shaft and it can be inserted in the lower limb secured with screws. Elementary computations revealed that gluing this part with a glue such as Threebond 1373, with a shear strength of $38.2 \cdot 10^6$ MPa would be more than sufficient. The triangular shape both reduces the inertia of the part and allows the screws with which the motor is attached to be fastened.

D.5 Motor

Since the motor shaft suspends the lower limb the shaft play must be limited. According to the motor specifications of the selected Faulhaber 4490 048BS, only radial play of at most 15 µm is present. This should however not be a major problem considering the specified lower limb stiffness of $3.6 \cdot 10^5 \frac{\mathrm{N}}{\mathrm{m}}$ combined with maximum loads of 30 N, results in 83 µm displacements. Also this play will not be directly in the drive train.

The dynamic friction coefficient of the motor is:

$$\begin{aligned} 1.0 \cdot 10^{-3}\,{}^{\mathrm{mNm}}/_{\mathrm{rpm}} &= 1.0 \cdot 10^{-6}\,{}^{\mathrm{Nm}}/_{\mathrm{rpm}} \\ &= \frac{60}{2\pi} \cdot 10^{-6}\,{}^{\mathrm{Nm}}/_{\mathrm{rad/s}} \\ &= 9.55 \cdot 10^{-6}\,{}^{\mathrm{Nm}}/_{\mathrm{rad/s}} \end{aligned}$$

which is an order of magnitude below the specified value. The motor constant is: $k_{\mathrm{e}} = 7.871\,\frac{\mathrm{mV}}{\mathrm{rpm}} = 7.516 \cdot 10^{-2}\,\frac{\mathrm{V}}{\mathrm{rad}}$, which results in an EMF of $U_{emf} = k_e\omega = 7.516 \cdot 10^{-2} \cdot 3.4 = 0.26\,\mathrm{V}$ where ω is the 95% interval highest motor speed, found in Figure B.7. The self-inductance of

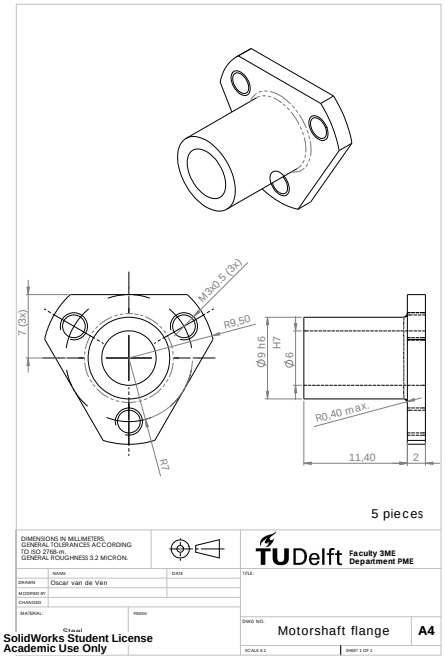

Figure D.6: Motor flange drawing.

Figure D.7: Motor flange picture.

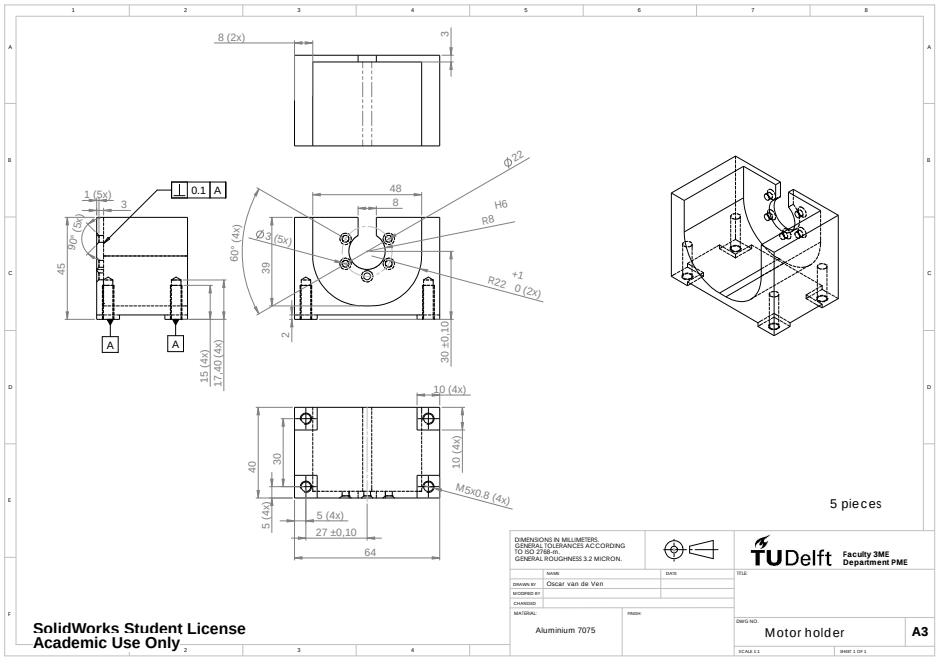

Figure D.8: Motor holder drawing.

the windings is $L_{\mathrm{w}} = 720\,\mu\mathrm{H}$, which means that to produce a sinusoidal current of 30 Hz (the control bandwidth) with an amplitude of the stall current (22.5 A), an extra voltage of $\overline{U} = \overline{I}\omega L = 3\,\mathrm{V}$ is needed. Finally the motor inertia is $1.30 \cdot 10^{-5}\,\mathrm{kgm}^2$ and the stall torque is 1.689 Nm.

D.6 Motor holder

The stiffness of the structure at the end of the lower limb is specified at $3.6 \cdot 10^5\,\frac{\mathrm{N}}{\mathrm{m}}$. Because the motor holder does not contribute to the effective inertia, the mass does not need to be limited. Therefore the stiffness should be an order of magnitude larger.

The motor suspension stiffness has been evaluated using finite elements in SolidWorks (see Figure D.9). The weakest deformation direction appeared to be the axial load. A 10 N load, which is the order of magnitude of the maximum expected loads, resulted in a deformation at the lower limb end of approximately 1.5 µm, or an effective stiffness of $7 \cdot 10^6\,\frac{\mathrm{N}}{\mathrm{m}}$ which is sufficient. The stiffnesses in orthogonal directions are an order of magnitude larger, effective stiffness in torsional directions are marginally larger.

The design depicted in Figure D.8 allows the motor with the flange glued on the shaft to be removed through the slot. The four short legs on the bottom allow accurate placement on the base plate. The bottom circular part fits loosely around the motor, such that when applying a heat conductor in between, the motor heat can flow out easily. The manufactured design is shown in Figure D.11.

D.7 Encoder

The selected Scancon 2MCA encoder has a 5000 pulses or 10000 steps per revolution resolution [Sca11]. The static friction torque is specified at 5 mNm maximum and the inertia is $2 \cdot 10^{-8}\,\mathrm{kgm}^2$. The static friction torque is one of the main problems of the encoder, but

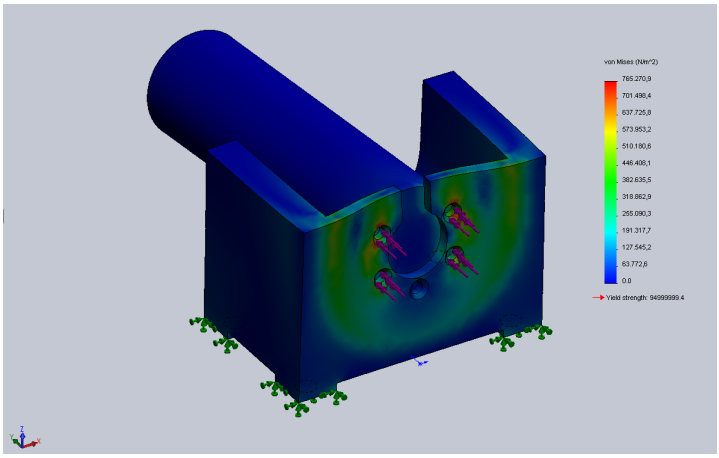

Figure D.9: Motor holder FEM analyses of the axial load, which appeared to be the weakest direction. The actual motor has a larger diameter than the rod shown in the analysis. This rod only connects the screw holes and is used to evaluate deformations.

it must be noted that all observed encoders of comparable resolution and price-range have typically these friction values. Apparently this is inherent to the build form needed to achieve this resolution. At higher prices though the friction can be lower, but the inertia is increased reducing the net benefit.

D.8 Encoder holder

The design of the encoder holder is a scaled down version of the motor holder. However the encoder holder has a specific cutout that accurately positions the encoder. The drawing is given in Figure D.10 and Figure D.11 shows both finished holders. Since the forces on the encoder are significantly lower than the forces on the motor and the stiffness is higher due to the scale, the deformations will not be significant.

D.9 Wire bus

The design of the wire bus is to a large extent based on the design found in the first prototype (Section 4.1). Only to eliminate the problem of the scratching wire, the diameter of the dent which guides the wire is now somewhat larger than the wire diameter: 0.6 mm while the wire is 0.5 mm. The wire bus will be glued on the encoder shaft.

D.10 Base plate

Since weight is not a major issue for the base plate, a 10 mm thick aluminium plate is used. The plate acts as a solid base for all parts and as a heat sink for the produced motor heat. The slots allow the lower limbs to reach large negative angles. To place the base plate at the required height a set of vertical plates is mounted underneath and placed on a circular disk. This provides extra mechanical stiffness to the base plate and can act as additional heat sink when manufactured from a good heat conductor such as aluminium.

To mount the encoder and motor holders, numerous holes have been made in the base plate. Note that the motors are placed at a larger distance than prescribed by the geometric

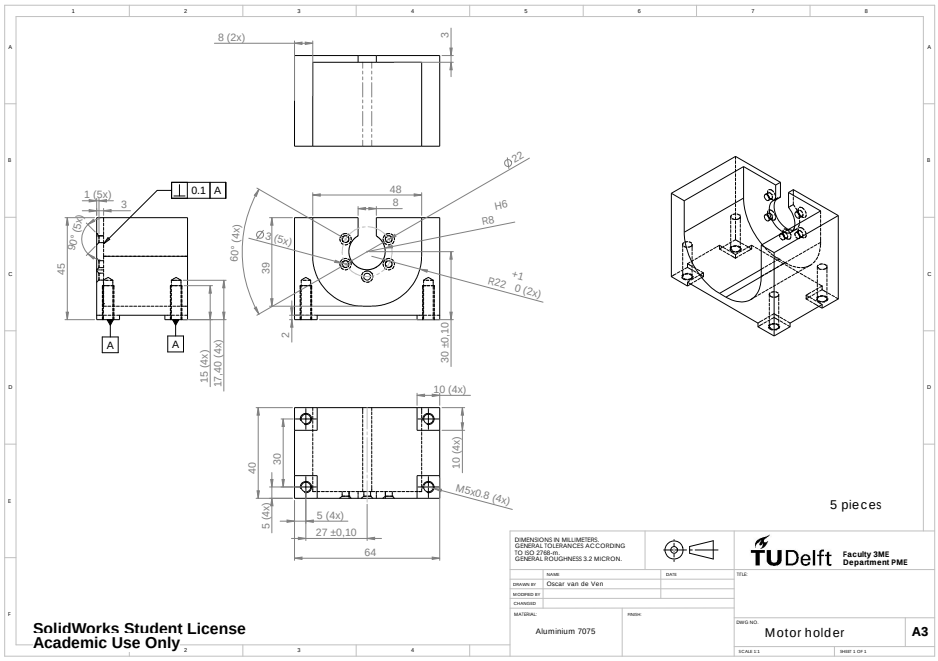

Figure D.10: Encoder holder drawing.

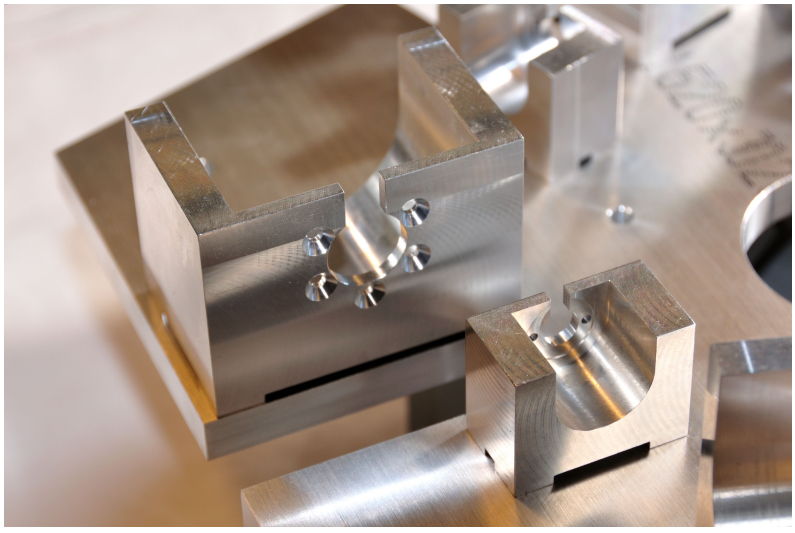

Figure D.11: Picture of the motor holder and the encoder holder placed on the base plate.

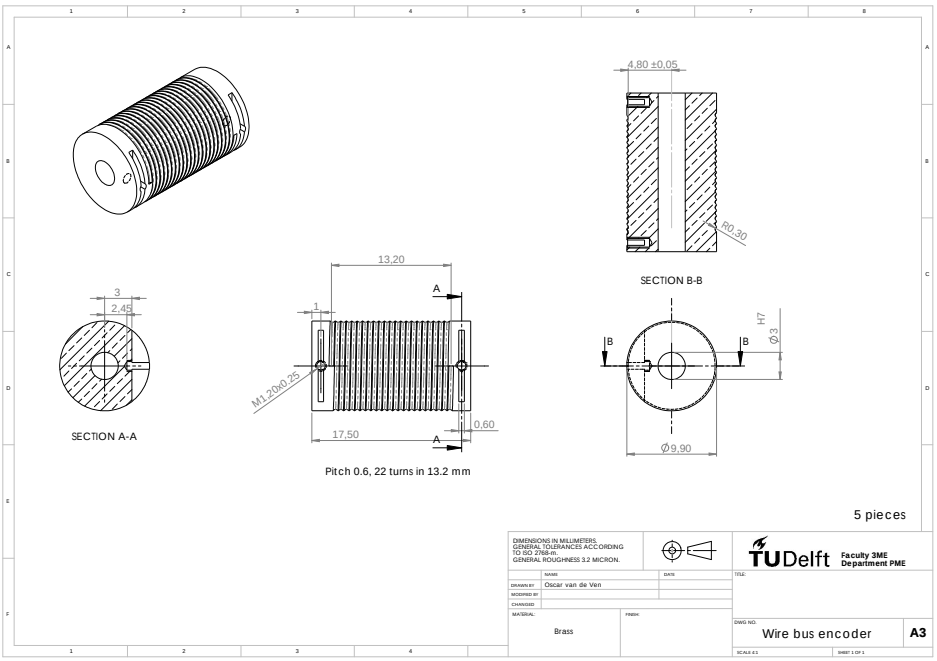

Figure D.12: Wire bus drawing.

Figure D.13: Picture of the manufactured wire bus. The slots to clamp the wire are still to be made.

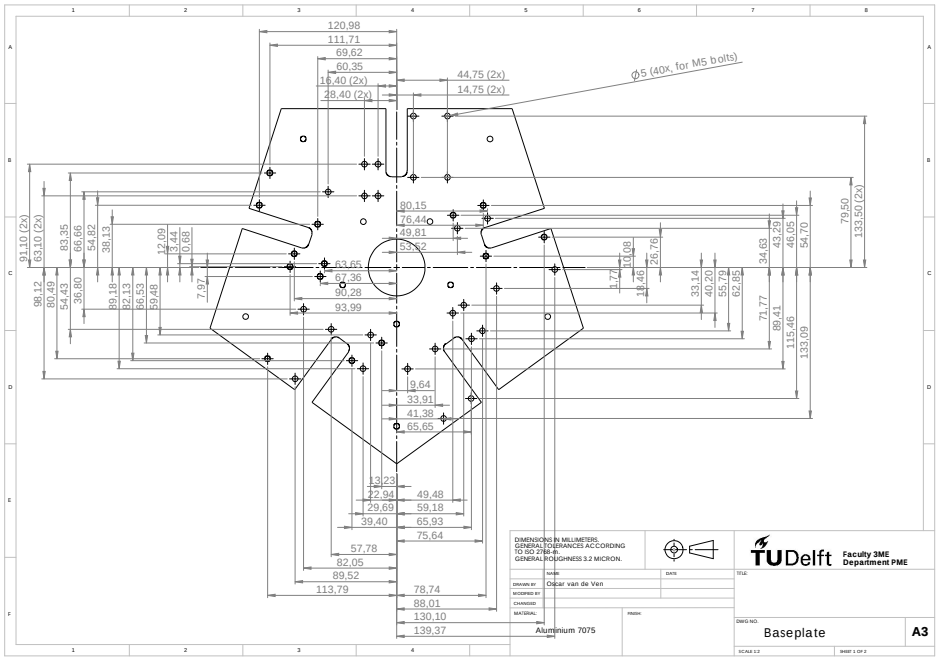

Figure D.14: Base plate drawing

Table D.1: Control card conversion times for 8 channels. Note that AD and DA conversion are done by the hardware on the background and do thus not cost computation time.

Task	Time
Analog output	1.35 μs
Encoder readout	4.72 μs
Analog readout	17.8 μs
Total	23.87 μs (42 KHz)

parameter (Appendix G) in order to compensate for an offset in the design of the a-links in the platform. This is described in [Vog11].

D.11 Control system

D.11.1 Interface card

Appropriate analog and digital interface cards of Quanser [Qua11] and National Instruments [Ins11] have been considered, as well as Softing CAN interfaces. The Quanser Q8 appeared to be the best over all solution.

The encoder timing is sufficient, since the maximum expected pulse-rate from the encoders is $5000\,\frac{\text{counts}}{\text{turn}} \cdot 4\,\frac{\text{pulses}}{\text{count}} \cdot 5 \cdot 3.4\,\frac{\text{rad}}{\text{s}} \cdot \frac{1}{2\pi}\,\frac{\text{turn}}{\text{rad}} = 5.4 \cdot 10^4\,\frac{\text{pulses}}{\text{s}}$ and the Q8 allows 8 MHz when using 4 quad-counts. The other timing performances are summarized in Table D.1.

D.11.2 Amplifier

With a motor constant of $k_t = 7.516 \cdot 10^{-2}\,\frac{\text{N}}{\text{A}}$ and a motor stall torque of $\tau_{max} = \tau_{stall} = 1.689\,\text{Nm}$, the amplifier must be able to supply at least $I_{stall} = \frac{\tau_{stall}}{k_t} = \frac{1.689}{7.516 \cdot 10^{-2}} = 22.47\,\text{A}$. The Maxon DES 70/10 is able to do that with a peak current of 30 A.

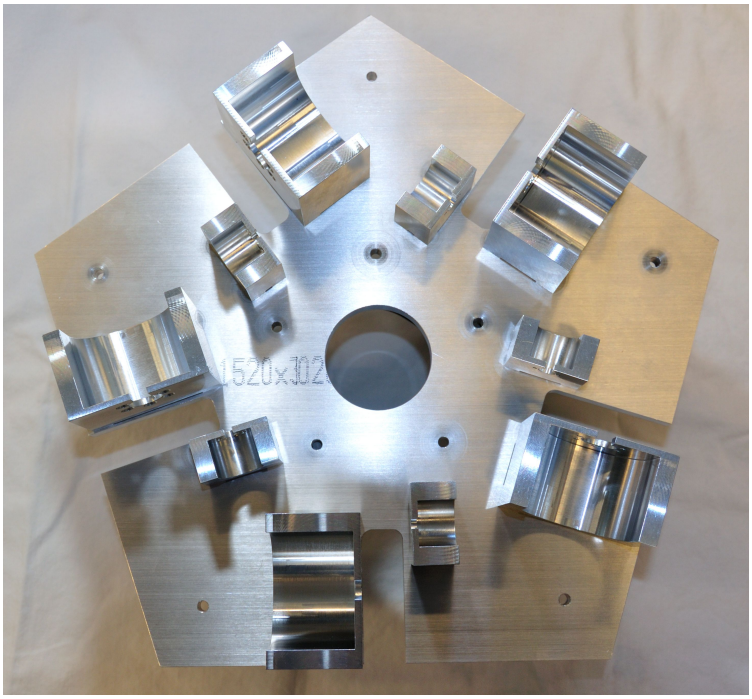

Figure D.15: Picture of the base plate with the motor and encoder holders.

D.12 System performance

An overview of the composition of the final actuator-sensor system performance is given next.

Inertia The inertia of the different parts is:

- Lower limb: $8.4 \cdot 10^{-5}\,\mathrm{kgm}^2$
- Lower limb plate: $1.1 \cdot 10^{-5}\,\mathrm{kgm}^2$
- Wire bus: $1.3 \cdot 10^{-7}\,\mathrm{kgm}^2$
- Flange: $2.2 \cdot 10^{-7}\,\mathrm{kgm}^2$
- Motor: $1.3 \cdot 10^{-5}\,\mathrm{kgm}^2$
- Encoder: $2.0 \cdot 10^{-8}\,\mathrm{kgm}^2$
- Cable: $3 \cdot 10^{-7}\,\mathrm{kgm}^2$

Therefore the total sensor-actuator system inertia is: $i^2\,(I_{\text{wire bus}} + I_{\text{encoder}}) + I_{\text{motor}} + I_{\text{flange}} = 1.7 \cdot 10^{-5}\,\mathrm{kgm}^2$, with $i = 5$. The lower limb inertia is excluded since this is already accounted for in the structural analysis in [Vog11]. Note however that the inertia of the lower limb of the first prototype is $1.4 \cdot 10^{-4}\,\mathrm{kgm}^2$ and that the limb length of the new prototype is larger. The cable inertia is estimated based on one winding around the large radius and 5 windings around the small radius.

Due to linearity of the computations the resulting fingertip force in the 95% interval can be derived from the results of Appendix B. This force is $9.1 \cdot 10^{-3}\,\mathrm{N}$. On average the maximum force on fingertip will be $4.7 \cdot 10^{-3}\,\mathrm{N}$ and $4.2 \cdot 10^{-3}\,\mathrm{N}$ for fingertips 1 and 2 and $5.1 \cdot 10^{-3}\,\mathrm{N}$ as a maximum of the fingertips.

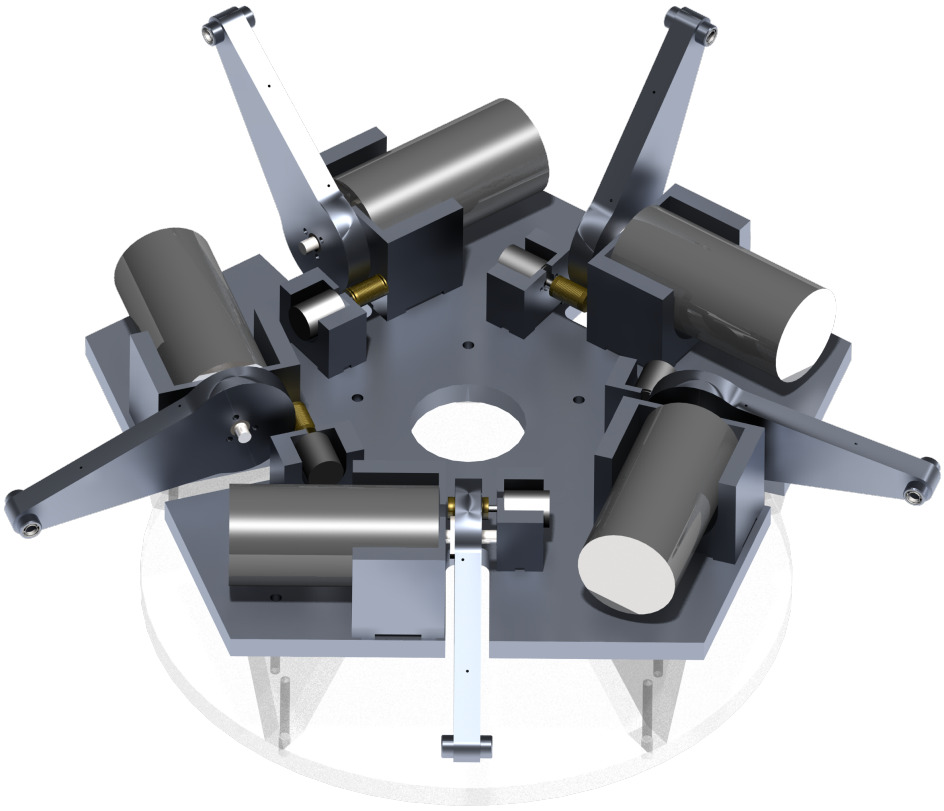

Figure D.16: Photorender of the assembled actuator and sensor system including the lower limbs.

Structure From [Vog11] it is known that the average force due to acceleration and velocity of the structure is 0.31 N, where the majority is due to inertia. The structure has a stiffness of $6.7 \cdot 10^3 \frac{\mathrm{N}}{\mathrm{m}}$ excluding the 5% worst case and $2.0 \cdot 10^4 \frac{\mathrm{N}}{\mathrm{m}}$ on average, both at the fingertips. At the maximum force and the average stiffness this means that the deformation will be 0.35 mm.

Dynamic friction Only the motor gives significant dynamic friction. The specified value is: $9.55 \cdot 10^{-6}\,{}^{\mathrm{Nm}}/_{\mathrm{rad/s}}$. This is in the 95% interval a force of $6.6 \cdot 10^{-4}\,\mathrm{N}$. The workspace average maximum force on fingertip is $3.4 \cdot 10^{-4}\,\mathrm{N}$ and $3.0 \cdot 10^{-4}\,\mathrm{N}$ for fingertips 1 and 2 and $3.7 \cdot 10^{-4}\,\mathrm{N}$ as the maximum of the fingertips is considered.

Static friction The known static friction contributions only come from the motor and the encoder:

- Motor: $3.65 \cdot 10^{-3}$ Nm
- Encoder: $5 \cdot 10^{-3}$ Nm

Including the transmission this sums up to: $2.9 \cdot 10^{-2}$ Nm. Note that the friction value of the motor is a maximum value, so this is the worst case scenario. In the 95% interval this is 1.2 N at the fingertips. On average this force is 0.87 N at fingertip 1 and 0.83 N at fingertip 2, both in the worst direction. The average of the maximum of both fingertips is 0.90 N.

Force The actuator is able to give a maximum torque of 1.7 Nm. At the end-effector this is 6.3 N in the 90% interval. On average the actuation system can give 10 N to both fingertips in any direction. The average force over all directions is 18 N.

Resolution The realized sensor resolution is $6.28 \cdot 10^{-5}\,\mathrm{rad}$, which is 0.1 mm in the 95% interval. The workspace average worst direction resolution is $2.0 \cdot 10^{-2}\,\mathrm{mm}$ and $2.6 \cdot 10^{-2}\,\mathrm{mm}$ for fingertip 1 and 2 and $2.7 \cdot 10^{-2}\,\mathrm{mm}$ as the largest of both is averaged.

Mass The masses of the parts are as follows:

- Actuator sensor system: 0.94 kg
  - Motor: 0.750 kg
  - Encoder: 0.015 kg
  - Motor holder: 0.130 kg
  - Encoder holder: 0.035 kg
  - Wire bus: 0.010 kg
- Base plate (excluding the support structure): 1.76 kg

Appendix E

Real-time computations

E.1 Simulink model

In Figure E.1 the main layout of the Matlab Simulink model that runs on the XPC-Target system is depicted. The kinematics, control, output and compensation blocks contains the Matlab implementation of the respective blocks described in Section 3.4.3 on the software structure. In the monitoring block the computed tip-coordinates are displayed on the XPC-Target screen and the safety block uses a memory structure monitor whether the actuator speed has reached a maximum speed to disable the machine and prevent damage. In the control block a number of demonstration controllers have been implemented:

- Actuator angle control
- x, y, z position control with θ and ρ free
- 5 DOF position control
- Constant force
- Virtual horizontal plane
- Application of external torque
- Application of external force

In order to use the Simulink model on the XPC Target machine, the model should contain the input and output blocks of the installed hardware, in this case the Quanser Q8. Also all code must be made compatible with the compilation process.

E.2 Absolute encoder positions

The position measurement system with which both prototypes are equipped are essentially only rotational encoders. The second prototype has encoders that have an index-pulse, but because of the transmission between the lower limb and the encoder, the stroke of the lower limb corresponds to multiple turns of the encoder, making the index-pulse unusable. Because the absolute angle of the lower limbs is crucial for kinematic computation an external means of defining the absolute position must be used.

The first prototype, which will initially be connected to this system, has however no encoder homing sensors. Therefore a knob is placed to physically define the extreme negative angle. A one-time calibration then defines the absolute angles relative to the horizontal state. For implementation of the second prototype the light barriers used for homing the encoder will be read out to define the absolute encoder positions.

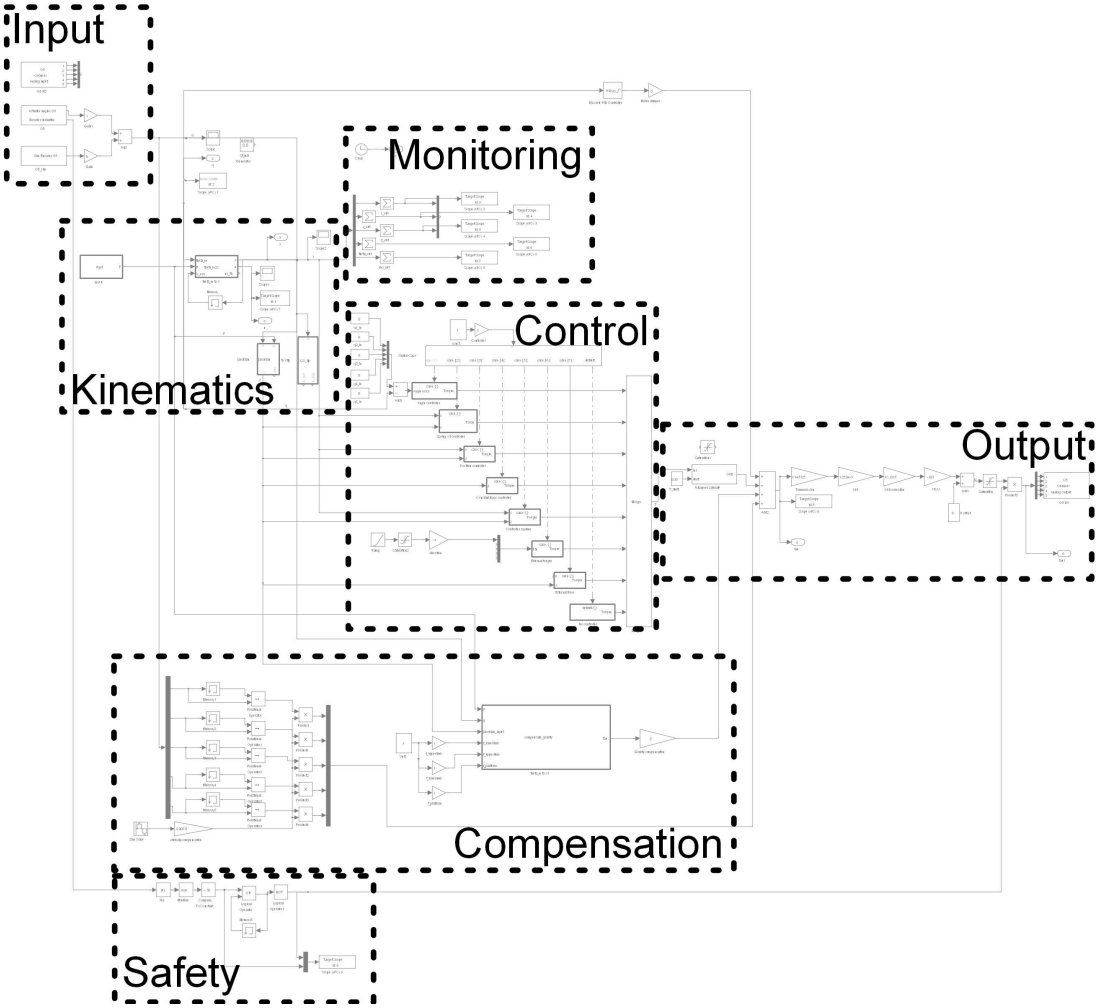

Figure E.1: Simulink model for the XPC Target system.

E.3 Forward kinematics

Since the forward kinematics cannot be solved analytically an iterative algorithm has been written to do this computation. In order to compute the forward kinematics (2.5)

$$\boldsymbol{\chi}(\boldsymbol{q}) = \mathbf{T}_{\text{fwd}}(\boldsymbol{q})\,\boldsymbol{q} \tag{2.5}$$

the velocity transfer of Equation (2.1) and the inverse kinematics in Equation (2.6) has been used:

$$\dot{\boldsymbol{\chi}} = \mathbf{J}\dot{\boldsymbol{q}} \tag{2.1}$$

$$\boldsymbol{q}(\boldsymbol{\chi}) = \mathbf{T}_{\text{inv}}(\boldsymbol{\chi})\,\boldsymbol{\chi} \tag{2.6}$$

Input data for this function are not only$\boldsymbol{q}$ but also an estimate of $\boldsymbol{\chi}$: $\boldsymbol{\chi}_{\text{est}}$The procedure is as follows:

- Start with a guess of the end-effector position $\boldsymbol{\chi}_{\text{est}}$. If the procedure is running for the first time, a value that results in good convergence for many points in space should be used. It appeared to be important to check for convergence of the actuator angles $\boldsymbol{q}$ connected to this starting value. This value is typically close the the center of the ellipsoidal workspace. In case of the first prototype it is: $\boldsymbol{\chi}_{\text{est},0} = \begin{bmatrix} 0 & 0 & 0.132 & 0 & 0.03 \end{bmatrix}^T$ m.
- Fill in $\boldsymbol{\chi}_{est}$ in the inverse kinematics function (2.6), this results in an estimate of $\boldsymbol{q}$: $\boldsymbol{q}_{est}$.
- Subtract the measured value of $\boldsymbol{q}$ of the estimate to obtain $\Delta\boldsymbol{q}$: $\Delta\boldsymbol{q} = \boldsymbol{q}_{\text{est}} - \boldsymbol{q}$.
- As in Section B.4, Equation (2.1) will be applied on small deviations of $\boldsymbol{q}$ and $\boldsymbol{\chi}$ instead of on their time derivatives: $\Delta\boldsymbol{\chi} = \mathbf{J}\Delta\boldsymbol{q}$.
- Compute a new estimate $\boldsymbol{\chi}_{\text{est,n+1}} = \boldsymbol{\chi}_{\text{est,n}} - \Delta\boldsymbol{\chi}$. The total equation of all step until this point is thus:
$$\boldsymbol{\chi}_{\text{est,n+1}} = \boldsymbol{\chi}_{\text{est,n}} - \mathbf{J}\left(\mathbf{T}_{\text{inv}}\left(\boldsymbol{\chi}_{\text{est,n}}\right)\boldsymbol{\chi}_{\text{est,n}} - \boldsymbol{q}\right)$$

This will be iterated until $\boldsymbol{\chi}$ is known with sufficient accuracy. The error is determined by the magnitude of $\Delta\boldsymbol{q}$ and must be smaller than the sensor resolution. If the computation error comes below this value the computation can be terminated.

Implementation of this algorithm on the first prototype shows that as long as the mechanism remains in the design-singularity the iteration needs in most cases between 1 and 3 steps to obtain an accuracy of 10^{-6} rad. The sensor resolution of this prototype is around $2.1 \cdot 10^{-4}$ rad, while the second prototype should obtain $6.3 \cdot 10^{-5}$ rad.

Appendix F

Rigid body model

The Matlab SimMechanics model of the PentaGriph mechanism, that has been developed in [vdVV11], is further expanded by modeling the actuator and sensor system and experimenting with elementary control of the robot. Also using data from [CA75] a simple kinematic model of the human arm and hand that can be connected to the robot is added. A picture of the layout of this model is given in Figure F.1.

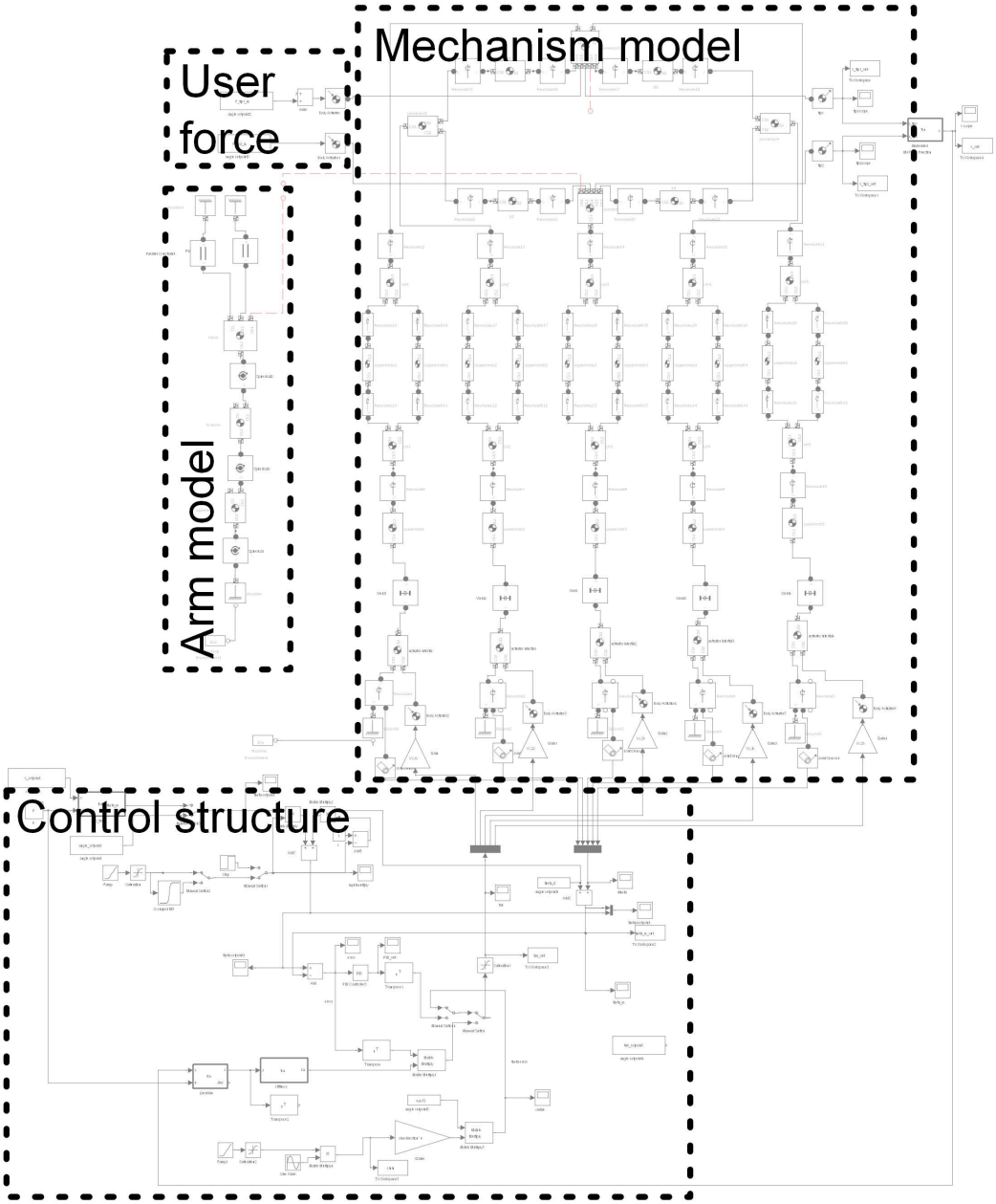

Figure F.1: Rigid body model of the PentaGriph robot in Matlab SimMechanics.

Appendix G

Geometric parameters

Table G.1 defines the geometric parameters of the PentaGriph mechanism used within the project. The first prototype is used to perform the measurements in Chapter 4. The second prototype parameters have been used in the analysis and the design. The a and b parameters describe dimensions of the platform parts, see [Vog11, Lam10] for more information.

Table G.1: Geometric parameters of the prototypes.

Parameter	First prototype	Second prototype
Base radius	70 mm	100 mm
Lower limb length	85 mm	90 mm
Parallelogram length	150 mm	200 mm
$a_{1,\mathrm{x}}$	28.75 mm	23 mm
$a_{1,\mathrm{y}}$	0 mm	0 mm
$a_{2,\mathrm{x}}$	-3.5 mm	-1.8 mm
$a_{2,\mathrm{y}}$	10.5 mm	5.3 mm
$a_{3,\mathrm{x}}$	-26.25 mm	-21 mm
$a_{3,\mathrm{y}}$	0 mm	0 mm
b_1	55 mm	48 mm
b_2	37.5 mm	30 mm

Appendix H

Hardware first prototype

The setup of the first PentaGriph prototype contains the following hardware:

Motor Maxon 310007 brushed DC, 24 V, 60 W

Encoder Maxon HEDS 5540, 500 Counts per turn, 3 Channels

Amplifiers Technosoft ISCM4805 DIN Intelligent Servo Module

Power supply TRACOPOWER - TSP 600-124, 24 V, 25 A

Fuses Regular blade type in holder, separate for logical and motor current

Cables

- **Encoders** 5 conductors + shield, DIN 5p to IDC 5p
- **Amplifier input** 2 conductors + shield, RCA to WAGO
- **Motor** $1.5\,\mathrm{mm}^2$ dual conductor
- **Power supply** $2.5\,\mathrm{mm}^2$ dual conductor

Iterface card Quanser Q8

PC system Dell OptiPlex 780

- **Processor** Intel Core 2 Quad Q8400 2.66GHz
- **Memory** 4GB (2x2048MB) 1333MHz DDR3
- **Hard-disk** 500GB S-ATA II 7200rpm

Bibliography

[CA75] R.F. Chandler and United States. National Highway Traffic Safety Administration, *Investigation of inertial properties of the human body: prepared for the u. s. department of transportation, national highway traffic safety administration*, National Technical Information Service, 1975.

[Com00] J.C. Compter, *Mechatronics introduction to electro-mechanics mass products & technologies*, Philips Centre for Industrial Technology, 2000.

[Dim11] Force Dimension, *Force dimension company website*, `http://www.forcedimension.com`, 2011.

[DM05] Manfred Becker Dieter Jannasch Joachim Vossiek Dieter Muhs, Herbert Wittel, *Roloff / matek machineonderdelen*, Academic Service, 2005.

[EKG09] B. Ebrahimi, M.B. Khamesee, and F. Golnaraghi, *A novel eddy current damper: theory and experiment*, Journal of Physics D: Applied Physics **42** (2009), 075001.

[FAST10] Inc. Futek Advanced Sensor Technology, *Futek company website*, `http://www.futek.com`, 2010.

[Fau11] Faulhaber, *Faulhaber company website*, `http://www.faulhaber-group.com/`, 2011.

[GH08] A. Gosline and V. Hayward, *Eddy current brakes for haptic interfaces: Design, identification, and control*, Mechatronics, IEEE/ASME Transactions on **13** (2008), no. 6, 669–677.

[HT11] Inc. H2W Technologies, *H2w technologies company website*, `http://www.h2wtech.com`, 2011.

[Ins11] National Instruments, *National instruments company website*, `http://www.ni.com/`, 2011.

[Kos05] M.P. Koster, *Constructieprincipes voor het nauwkeurig bewegen en positioneren*, Twente University Press, 2005.

[Lam10] P. Lambert, *A novel 5 dof fully parallel robot combining 3t1r motion and grasping*.

[Mer06] J.P. Merlet, *Parallel robots*, Springer-Verlag New York Inc, 2006.

[MHRH09] G. Millet, S. Haliyo, S. Regnier, and V. Hayward, *The ultimate haptic device: First step*, Proc. and Symp EuroHaptics conference Haptic Interfaces for Virtual Environment and Teleoperator Systems. World Haptics 2009. Third Joint, 2009, pp. 273–278.

[Mot10] Maxon Motor, *Maxon motor company website*, `http://www.maxonmotor.com`, 2010.

[Nov11] Novint, *Novint company website*, `http://www.novint.com`, 2011.

[Qua11] Quanser, *Quanser company website*, `http://www.quanser.com`, 2011.

[Sca11] Scancon, *Scancon company website*, `http://www.scancon.dk`, 2011.

[SMT10] Inc SL Montevideo Technology, *Sl montevideo technology, inc company website*, `http://slmti.com/`, 2010.

[Tec10] Interlink Electronics Sensor Technologies, *Interlink electronics company website*, `http://www.interlinkelec.com`, 2010.

[Tek10] Tekscan, *Tekscan company website*, `http://www.tekscan.com`, 2010.

[TvD11] Just L. Herder Teunis van Dam, Patrice Lambert, *Static balancing of translational parallel mechanisms*, Proceedings of the ASME 2011 International Design Engineering Technical Conferences & Computers and Information in Engineering Conference IDETC/CIE 2011 (2011).

[vdVV11] O.S. van de Ven and J.G. Vogel, *Human specifications and computation tools for a 5 dof parallel haptic robot.*, Tech. report, TU Delft, 2011.

[Vog11] J.G. Vogel, *Conceptual and detailed structural design of a 5 dof parallel haptic robot*, Master's thesis, TU Delft, 2011.

[Wik11] *Wikipedia*, `http://www.wikipedia.org`, 2011.